Geometrically-engineered human motor assembloids-on-a-chip for neuromuscular interaction readout and hypoxia-driven disease modeling

Check for updates

Weihua Zhang [1,2,4], Liming Yu[1,2,4], Jie Pan [1,2,4], Jiajia Deng[1,2], Xianqin Tong[1,2], Bingjiao Zhao[1,2], Wen Liu[1,2], Liangyan Sun[1,2], Menghan Zhang[3], Xinxin Han[1,2], Tingjiao Liu[1,2], Yun Lu [1,2] ✉, Jiao Li [1,2] ✉ & Yuehua Liu [1,2] ✉

Precision medicine leverages stem cell-derived models to dissect complex interactions underlying disease-driven neuromuscular damage. However, such reductionist models form stochastic structures without external guidance, while available engineering solutions remain intricate. Here, simplified surface modification engineering is used to render spatially patterned human motor assembloids-on-a-chip by geometric confinement. The anisotropic architecture of skeletal muscle organoids (hSkM) can be conferred solely by localized mechanobiological cues within this predefined device without aligned scaffolds or adjuncts. The hSkM-orchestrated coupling of motor neuron spheroids (hMNS) promotes synergistic neuromuscular development. Furthermore, integration of optogenetic and microelectrode array mapping enables visualization of functional patterning in assembloids. Applied to oxygen deprivation model, hSkM exhibits structural anomalies, fatigable muscle remodeling and dysfunction, recapitulating muscle pathologies in intermittent hypoxia (IH)-associated respiratory disorders. Electrical activity mapping reveals the heterogeneity in neuromuscular responses to IH, indicating the neuroregulatory etiology of muscle dysfunction. Finally, we identify mitochondrial bioenergetic imbalance as a key IH target, proposing evaluation of NAD^+ salvage pathway-targeting agents. Our findings provide an accessible platform with translational potential for neuromuscular physiopathology research.

The neuromuscular system, fundamental to human motor functions including locomotion and breathing, is governed by motor units that assemble motor neurons and their innervated skeletal muscle fibers. To support these activities, oxygen supplies the essential energy needed for efficient neural signal transmission and muscle response[1].

However, pathological hypoxia, notably intermittent hypoxia (IH), compromises the physiological regulation of the neuromuscular system. IH serves as a pathological hallmark shared among various respiratory disorders, including obstructive sleep apnea (OSA)[2,3], chronic obstructive pulmonary disease (COPD)[4,5], and COVID-19[6].

[1]Department of Orthodontics, Shanghai Stomatological Hospital & School of Stomatology, Fudan University, Shanghai, China. [2]Shanghai Key Laboratory of Craniomaxillofacial Development and Diseases, Fudan University, Shanghai, China. [3]Stomatology Hospital, School of Stomatology, Zhejiang University School of Medicine, Zhejiang Key Laboratory of Oral Biomedical, Hangzhou, China. [4]These authors contributed equally: Weihua Zhang, Liming Yu, Jie Pan. ✉e-mail: luyun@fudan.edu.cn; jiaoli@fudan.edu.cn; liuyuehua@fudan.edu.cn

Unlike persistent hypoxia, IH characterized by cyclical oscillations between normoxia and hypoxia, induces cellular and tissue stress responses, causing metabolic energy imbalances and oxidative damage[1,7]. Patients often suffer from complications like muscle fatigue and reduced physical capacity[8,9], with potential denervation phenotypes in muscle fibers such as atrophy and pathological subtype shifts[10,11]. These subtype shifts represent dysregulated fiber type remodeling, characterized by preferential loss of fatigue-resistant oxidative fibers[12]. The involvement of ventilatory muscles is particularly concerning, as it strongly correlates with disease progression and unfavorable outcomes[13,14]. Nevertheless, current studies have yet to uncover direct evidence of how IH affects human muscle pathology and neuroregulation, attributed to: (i) interference from other contributing factors besides IH; (ii) the complexity of identifying specific affected cell types within multi-tissue systems; and (iii) limitations in the clinical translation of animal models due to interspecies variations. Therefore, establishing a stable in vitro neuromuscular research platform with human physiological relevance has emerged as a priority for IH disease modeling and therapy. This imposes prospective requirements on the biofidelity, architectural features, and functional assessment of models.

As a complement to in vivo studies, neuromuscular study models have evolved from two-dimensional cultures to three-dimensional (3D) microphysiological systems, broadening their potential applications in precision medicine and disease modeling. Organoids, as cutting-edge tools in these systems, excel in replicating complex physiological structures and tracking multi-tissue dynamics[15]. To date, neuromuscular organoids[16] and cortico-motor assembloids[17] have been developed to model neuromuscular development and diseases in vitro, equipped with essential motor neuron physiological features and innervated skeletal muscle function. However, these models are typically based on 3D cell aggregates formed through stochastic self-organization, and their spatial arrangement requires further refinement. Beyond providing 3D space and specified cell types, specific tissue architectures serve as the key to functional biomimetics[18]. This is because tissues such as muscle demonstrate direction-dependent mechanical and electrical properties. Anisotropic muscles not only optimize movement and mechanical efficiency[19] but also facilitate signal integration in motor neurons[20]. Thus, engineering the morphology and structure of organoids can authentically replicate the neuromuscular physiological environment, which is imperative to improve the accuracy of models in predicting disease responses.

The need for preclinical human models has spurred the development of organoid-on-a-chip platforms that integrate bioengineering concepts to mimic tissue microenvironments. Recent technological advancements, such as microfabrication designed for aligning muscle fibers[21], 3D printing[22], and hydrogel or nanoscale scaffolds[23]—have improved model controllability and physiological fidelity to a certain degree. However, these methods require sophisticated equipment and complex fabrication, which compromises the accessibility and cost of platform application, posing challenges to widespread adoption across diverse laboratory settings.

Here, we reported a readily fabricated human motor assembloids-on-a-chip platform. By implementing surface modifications in specific regions of polydimethylsiloxane (PDMS) devices, we established differential tissue adhesion strengths, creating geometric constraints that promote localized biomechanical microenvironments. This simple approach allowed us to develop spatially patterned human motor assembloids-on-a-chip (Fig. 1a). Anisotropic human skeletal muscle organoids (hSkM) and human motor neuron spheroids (hMNS) self-organized during development to attain structural integration and functional connections. These components interact to exhibit a robust neuromuscular transcription profile. As a proof-of-concept application, we subjected the model to IH using previously established in vitro oxygen cycling conditions[24], demonstrating that the model recapitulated clinical phenotypes of muscle dysfunction observed in respiratory disorders. Furthermore, electrical activity mapping revealed that IH induced suppression of motor neuron firing and abnormal disturbances in their innervated myofibers, providing insights into neuromuscular interaction abnormalities from a neuroetiological perspective that are challenging to detect clinically. Finally, we also pinpointed mitochondrial bioenergetic imbalance, particularly in nicotinamide adenine dinucleotide (NAD$^+$) metabolism, as a key target of IH damage and assessed the efficacy of various pharmacological interventions. Therefore, human motor assembloids-on-a-chip emerge as a simple, efficient, and reliable platform for advancing neuromuscular pathology research and therapeutic development.

Results

Geometric engineering and generation of the human motor assembloids-on-a-chip

We first generated spheroids resembling the human motor nervous system from human induced pluripotent stem cells (hiPSCs), selecting P15-P25 hiPSCs with confirmed chromosomal stability by karyotype analysis for organoid generation (Supplementary Fig. 1b). Based on the fate patterning of spinal motor neuron development, we sequentially applied specific signaling molecules to induce hiPSCs[25]. The initial treatment with a Wnt activator and dual Smad inhibitors resulted in the emergence of rosette-like neural epithelial clusters after 5 days. These clusters began to express neuroepithelial progenitors (NEP) markers PAX6, PAX7, NESTIN, and NEUROD1, with a concurrent reduction in rostral fates (Fig. 1b and Supplementary Fig. 1a). To acquire ventral identity, the clusters were subsequently treated with RA and SHH agonists while decreasing Wnt signaling, enhancing their neural tube-like morphology. By day 10, both ventral and dorsal identities were confirmed through immunofluorescence and qPCR, yielding OLIG2+ motor neuron progenitors (MNP, 84.17%) expressing NKX6.1 (Fig. 1b and Supplementary Fig. 1c, d). The MNPs acquired at this stage could be passaged and cryopreserved. On day 16, MN maturation was enhanced by administering γ-secretase inhibitors and neurotrophic factors at least 8 days. Analysis on day 24 revealed ISL1 and HB9 positivity in MN, along with increased mRNA levels of mature markers such as ChAT, LHX3, and SYN (Fig. 1b and Supplementary Fig. 1e), suggesting features associated with the lateral motor columns. To generate motor neuron spheroids (MNS), MNP colonies were harvested and transferred to ultra-low attachment plates, maturing over time to diameters of $250 \pm 50 \, \mu m$. Meanwhile, electrophysiological recordings confirmed firing properties consistent with mature neurons (Fig. 1c and Supplementary Fig. 1f).

After obtaining hMNS, the next step was to develop devices for guiding the formation of anisotropic human skeletal muscle organoids (hSkM). In vivo, skeletal muscles terminate at bone surfaces, where mechanically induced tension during development serves as the biophysical basis for fiber orientation[26]. To this, our design incorporated geometric considerations, featuring semicircular endpoints on the patterns to mimic natural muscle anchoring, while addressing the need for experimental flexibility and throughput (Supplementary Fig. 2a). Importantly, key features of tissue anisotropy were recapitulated by implementing PDMS surface modifications in specific regions (Supplementary Fig. 2b). The middle region of the device was pretreated with Pluronic-127 to form a hydrophilic barrier that prevented nonspecific adhesion. Conversely, heterobifunctional crosslinker Sulfo-SANPAH acted as a "bi-adhesive", covalently binding to the PDMS surface upon photolysis, and mediating linkage between the functionalized surface of anchoring points in the device and the ECM proteins in cultures (Supplementary Fig. 2b, c). Next, the cell-laden biomatrix was seeded onto the pretreated device, matching with the device pattern. Continuous morphological monitoring showed the middle tissue progressively
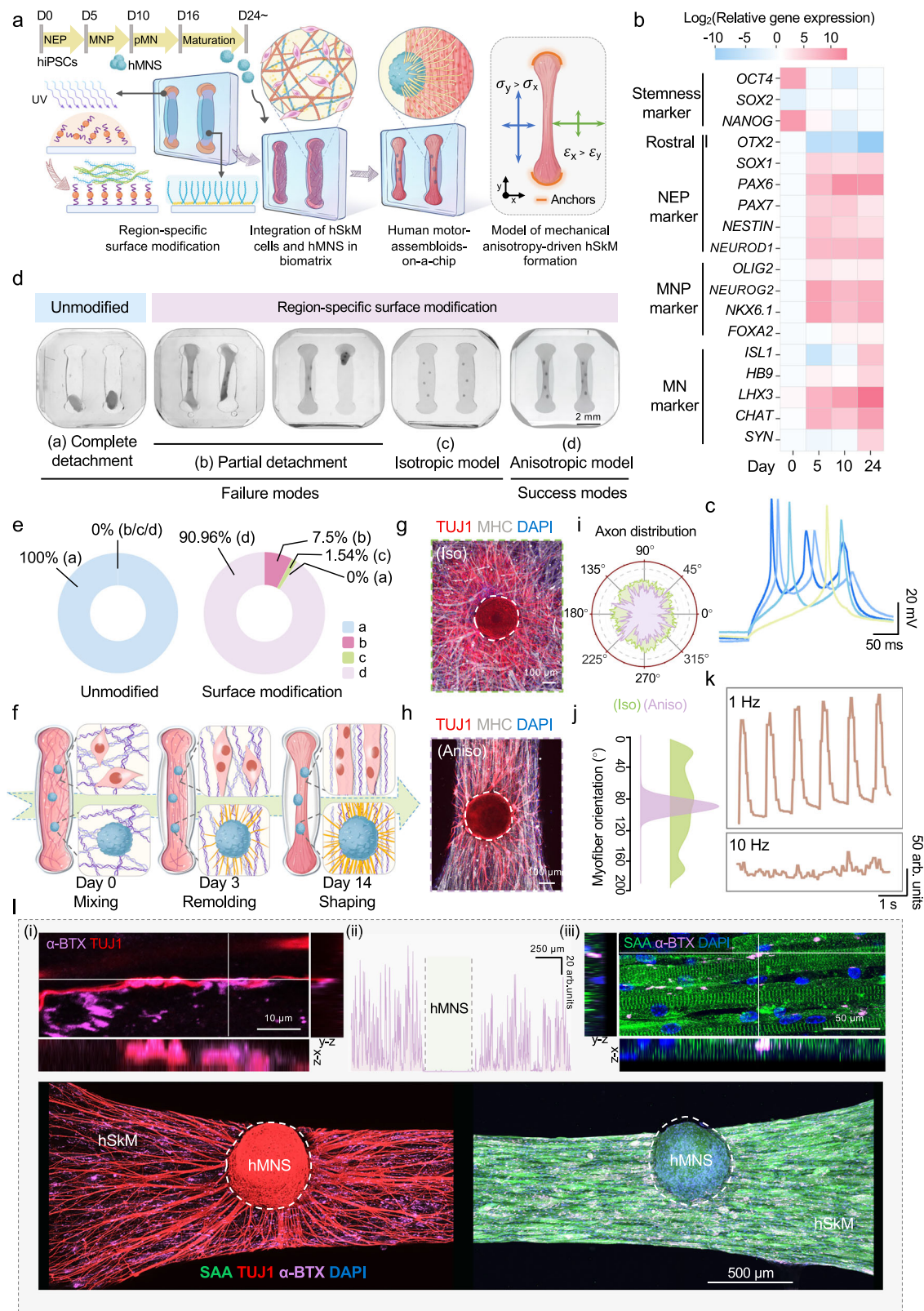
detaching from PDMS, moving towards contraction and linearization. At day 14, the tissue organized into aligned myobundles along the anchoring axis, with stable attachment to the PDMS surface at anchoring points (Supplementary Fig. 2e). These results confirmed that boundary constraints imposed by the pretreated device triggered localized anisotropic regulation of stress and strain within the tissue. The positions of the anchoring points provided directional

cues for muscle fiber polarization, while tissue mechanical tension guided local deformation and the orientation of self-organization, ultimately achieving a balanced skeletal muscle geometry.

To systematically assess the effect of surface modifications on the formation of geometric morphologies and attachment stability under biomechanical cues, hSkM and hMNS were assembled on the device, with each hSkM seeded with 3-4 evenly distributed hMNS

Fig. 1 | Geometric engineering and generation of the human motor assembloids-on-a-chip. a Schematic of the geometric confinement, assembly processes, and mechanical anisotropy mechanisms for human motor assembloids-on-a-chip. **b** Heatmap of the temporal expression patterns of developmental markers over 24 days during the generation of hMNS. *n* = 3 independent experiments. **c** Whole-cell current-clamp recording of action potential induction from a neuron within hMNS in response to depolarizing currents. **d** and **e** Anchoring and geometric configurations of motor assembloids. Representative images showing models of failure and success as defined in our research (**d**), along with quantification of these events (**e**). Unmodified: *n* = 4 independent experiments, Surface modification: *n* = 5 independent experiments. **f** Schematic representation of ECM alignment and tissue sculpting progression over 14 days. **g** and **h** Representative immunofluorescence of motor assembloids showing muscle fiber and axon orientation in isotropic and anisotropic models, stained for myosin heavy chain (MHC; gray), β-III tubulin (TUJ1; red), and nuclei (blue). **i** and **j** Dominant directions of axon (i) and myofiber (j) orientation in isotropic and anisotropic models. *n* = 3 assembloids. **k** Displacement trace of hSkM contractions in response to electrical stimulation at 1 Hz and 10 Hz. **l** Immunofluorescence analysis of the motor assembloid reveals hMNS projecting TUJ1 + axons (red) into the organized striated muscle region marked by sarcomeric α-actinin (SAA; green). (i) co-localization of an axon terminal with an AChR cluster labeled by α-bungarotoxin (α-BTX; magenta); (ii) distribution of AChR clusters surrounding hMNS; (iii) localization of AChR clusters on the striated muscle fibers. Three independent experiments was repeated independently with similar results. Source data are provided as a Source Data file.

(Supplementary Fig. 2f). We defined criteria for successful assembloid formation as follows: (i) assembloids in anchoring region remained firmly attached to PDMS without apparent detachment by the pre-determined day; (ii) hSkM in the middle region detached from the PDMS surface and suspended, forming bundles under mechanical stress; (iii) all assembloids within the same device remained securely attached to chamber without falling off; (iv) hMNS and hSkM were cohesively bonded without loosening or separation. Devices that lacked pre-treatment for surface modifications experienced total detachment and aggregation of assembloids by day 3, resulting in loss of skeletal muscle geometry. However, implementing specific regional surface modifications in the device, following our trouble-shooting guide (Supplementary Fig. 2d), effectively averted these issues. At day 14, only 7.5% of the assembloids displayed partial detachment in the anchoring region, and 1.54% of the middle region showed no delamination or compression. Notably, up to 90.96% of the assembloids gradually shaped and contracted, successfully forming myobundles that remained stably attached (Fig. 1d, e and Supplementary Fig. 2g). Furthermore, we compared myobundle stability and formation success rates among different anchoring methods (Frame and Micropillar) to evaluate our approach (Supplementary Fig. 3a). The results showed no statistically significant differences among the three models, with all achieving high average success rates (Supplementary Fig. 3b, c). Notably, however, we observed that the surface modification method achieved the highest frequency of 100% success rate batches across multiple experimental runs (75% vs. 50% vs. 25%) and exhibited the lowest coefficient of variation (8.05% vs. 12.50% vs. 13.84%) (Supplementary Fig. 3d). Therefore, this method may possess superior batch-to-batch stability, suggesting its potential value in scaled applications.

Similar to the properties of natural muscle, the attachment positions dictated the directionality of myocyte fusion. Applying surface modifications to the entire region (Supplementary Fig. 2h) resulted in an isotropic architecture of myofibers. Conversely, in the same geometric model but with localized surface modifications, the myofibers formed a highly organized anisotropic architecture (Fig. 1g, h and j). The directionality of muscle movement was further examined. hSkM displayed uniaxial twitching with a positive force-frequency relationship by electrical stimulation (Fig. 1k and Supplementary Movie 1). However, the axon outgrowth of hMNS coupled with hSkM showed no directional consistency in either model (Fig. 1g–i). Over the temporal sequence, the arrangement of myofibers received directional guidance through surface modification, whereas the growth paths of neuronal projections remained independent, constrained only by the length of the geometric boundaries (Fig. 1f). Nevertheless, axon outgrowth was more accentuated in anisotropic groups at the same longitudinal extent (Supplementary Fig. 2i–k).

The maturation of the neuromuscular system involves refining myofiber structure and the precise deployment of axons. Sarcomeric α-actinin (SAA) staining revealed that, after 14 days, the muscle cells in the assembloids had coalesced into highly organized, multinucleated

fibers with typical striations of sarcomere organization (Fig. 1l (iii)). Concurrently, hMNS extended TUJ1 + axons exhibiting a radially centered distribution with abundant branching, tightly adhering to the hSkM surface (Fig. 1l bottom). Neuromuscular junction (NMJ) formation is crucial for motor neuron-mediated muscle contractions and is integral to neural signal transmission. The connection between MN and muscle was preliminarily assessed by α-bungarotoxin (α-BTX) labeling of acetylcholine receptor (AChRs) density and distribution, revealing that AChR clusters were dispersed around the hMNS (Fig. 1l (ii)). Notably, 3D projection verified that, along the z-axis, the formation of NMJ by TUJ1+ axon terminals co-localized with α-BTX+ AChRs (Fig. 1l (i)), indicating that these myofibers were structurally innervated by motor neurons.

Co-emergence and coupling of functional components in human motor assembloids supported neuromuscular development

To investigate the crucial role of neuromuscular interactions in the maturation and functional optimization of motor assembloids, we constructed different assembly models of hMNS and hSkM (Fig. 2a). The introduction of hMNS led to a significant enhancement in expression of type I and type II myosin heavy chains (MHC-I and MHC-II) in hSkM, particularly in the later stages of development (Fig. 2b, c and Supplementary Fig. 4f). The gene expression of type II muscle fibers, which is linked to high endurance and oxidative metabolic abilities, increased from day 7 onwards (Fig. 2d). This indicates a key regulatory role of neural signals in driving muscle cell differentiation toward specific subtypes. In addition, the higher expression levels of muscle contraction-related proteins such as SAA, pan-MHC, and myosin light chain (MYL) in the assembloids group suggested improved muscle function and organoid maturity (Fig. 2b, c). Furthermore, NMJ formation and function were optimized, as demonstrated by the upregulation of AChR subtypes CHRNA1 and CHRNB1 (Supplementary Fig. 4a–c), and the calcium-modulating protein CASQ1 (Supplementary Fig. 4d, e). Importantly, we also found that skeletal muscle exerted retrograde regulation on motor neuron development. Although other studies have presented similar data on the promotive effects of nerves on muscle maturation[27,28], few have explored the retrograde influence of muscle on neuron. We observed that in the presence of hSkM, the diversity of MN subtypes in hMNS was enhanced, with higher expression levels of genes associated with fast and slow MN (Fig. 2e). This bidirectional synergistic interaction highlights the importance of neural and muscle tissues in organoid maturation and functional optimization.

To further clarify how neural innervation propels the self-assembly and co-development of motor assembloids rather than mere co-culture, we designed a non-hMNS-innervated hSkM model and an hSkM-hMNS assembloid. Bulk RNA-seq analysis showed substantial expression differences between the two models. Comparison of volcano plots revealed that 3364 genes were upregulated and 2334 genes were downregulated in the innervated model, indicating
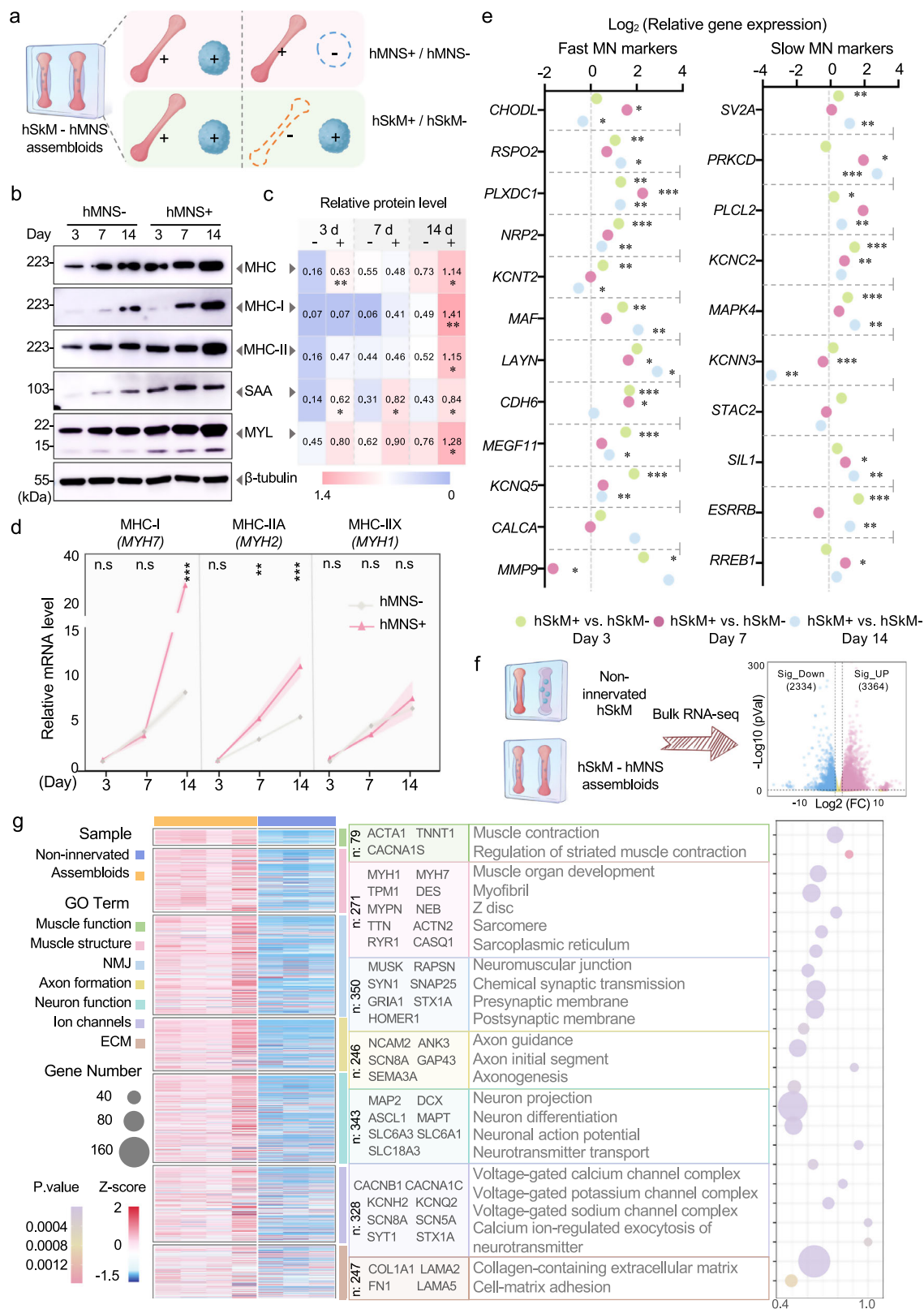
extensive gene expression regulation during motor assembloid self-assembly (Fig. 2f). To dissect the specific transcriptomic features contributing to motor assembloid formation, we analyzed differential expression between the two models. Compared to the non-hMNS-innervated hSkM model, motor assembloids were enriched with genes involved in muscle (e.g., *ACTA1, TTN, DES*) and NMJ development (e.g., *MUSK, RAPSN, SYN1*). Moreover, the assembloids

showed higher gene expression linked to neural developmental procedures, including axon formation and neuronal processes (e.g., *NCAM2, MAP2, DCX*). The upregulation of genes linked to ion channels and extracellular matrix components further underscored the criticality of cellular electrical signaling and tissue structural stability (Fig. 2g). Overall, motor assembloids possess a robust neuromuscular transcriptomic profile, supporting that motor assembloids

Fig. 2 | Synergistic development of functional components in motor assembloids. a Schematic illustrating experimental setups for motor assembloids to explore interactions between hSkM and hMNS. **b** and **c** Representative western blots (**b**) and heatmap profiles (**c**) showing the protein levels of MHC, MHC-I, MHC-II, sarcomeric α-actinin (SAA) and myosin light chain (MYL) in organoids with or without hMNS over 14 days. with β-tubulin as loading control. $n = 3$ independent experiments. **d** Gene expression (RT-qPCR) of myosin complex-related markers over 14 days in organoids with or without hMNS, normalized to 18S. $n = 3$ independent experiments. **e** Relative gene expression of motor neuron subtype-related markers in organoids with or without hSkM over 14 days. $n = 3$ independent experiments. **f** Schematic of the model of non-innervated hSkM organoids ($n = 3$ organoids) and hSkM-hMNS assembloids ($n = 4$ assembloids), with a corresponding volcano plot showing differential gene expression from bulk RNA-seq. **g** Heatmap with gene ontology (GO) enrichment annotations illustrating differential gene expression and functional categorization in non-innervated organoids and motor assembloids. Data are presented as mean ± SD. Statistical analysis: **e** two-tailed Student's t test. **b**, **d** Two-way ANOVA with Bonferroni multiple comparison. $^{***}p < 0.001$, $^{**}p < 0.01$, $^{*}p < 0.05$. Source data are provided as a Source Data file.

development and maturation rely on neuromuscular interactions driven by functional unit coupling.

Function characterization of human motor assembloids

Motor neuron-driven muscle movements constitute the fundamental functional output of the neuromuscular system. Following the initiation of motor assembloid assembly, spontaneous twitching of the muscles was noted. To compare contraction activity patterns across different regions, the area surrounding the hMNS was delineated with yellow dashed lines, subdividing it into several observation subregions within and equal subregions outside the dashed boundaries. Motion displacement analysis of these imaging subregions revealed that spontaneous contraction displacement was greater proximal to the hMNS compared to distal regions (Fig. 3a and Supplementary Movie 2). In addition, heatmap analysis further validated that the primary zones of spontaneous contraction were centralized around the hMNS in the motor assembloids (Fig. 3b). As the differentiation progressed, the frequency of spontaneous contractions was recorded, starting on day 3, peaking at 34.4% by day 5, and then decreasing steadily until day 14 (Supplementary Fig. 5a). Spontaneous contractions were mainly captured during the early stages of assembly (Fig. 3c), a phase involving myocyte fusion or the initial formation of NMJ, as previously reported in 3D cultures in vitro[29].

Following assembly, axon projections of the motor assembloids densified and expanded progressively (Fig. 3d). We next assessed key physiological parameters of the mature motor assembloids using glutamate and optogenetics to characterize the functional connectivity between hMNS projections and hSkM. First, we used the caged excitatory neurotransmitter glutamate to probe NMJ connectivity, a method that activates MN without affecting the muscle. Upon light exposure (405 nm), caged glutamate releases glutamate that interacts with specific receptors (Supplementary Fig. 5b). This resulted in muscle twitching in the analyzed subregions, which was blocked by curare treatment and not related to light stimulation (Supplementary Fig. 5c). In the absence of caged glutamate, light exposure failed to elicit responses in the motor assembloids. For more precise and broader manipulation, optogenetics was employed. hChR2 (H134R) was delivered into hMNS via a lentiviral vector prior to assembly (Supplementary Fig. 5d, e), with strong expression maintained for 2 weeks (Fig. 3f). Blue light (473 nm) stimulation triggered synchronous muscle contractions both locally and throughout the broader hMNS regions (Fig. 3e, Supplementary Fig. 5g and Supplementary Movie 3).

Next, we integrated optogenetics with a microelectrode array (MEA) to visualize the electrical activity in motor assembloids (Supplementary Fig. 5f), pinpointing the origins of the electrical signals detected at each electrode (Fig. 3g). MEA monitoring revealed that electrodes within the assembloids region detected synchronized spike responses across multiple electrodes upon optogenetic stimulation. Further analysis confirmed these synchronous events, revealing the highly coherent spatiotemporal propagation of electrical activity within the motor assembloids (Fig. 3h, i and k). When the optical stimulation was ceased, remaining electrical activities on some electrodes no longer exhibited the previous synchrony (Supplementary

Fig. 5h). Such synchronous output not only confirmed the functional connectivity between hMNS and hSkM but also showcased that our motor assembloids can mimic the coordinated responses typical of neuromuscular systems. To visualize the spatial readouts of motor assembloid activities, we mapped the electrical activity based on functional unit positions on the electrodes and performed an analysis of firing events and amplitudes. Node-level tags in this map denoted the spike count and average amplitude recorded by each electrode during the recording. Optogenetic stimulation of these assembloids manifested electrical activity in the hSkM regions (Fig. 3j and Supplementary Fig. 5i (left)), providing concrete evidence for the controllability of NMJ function. Administration of curare effectively abolished these optically evoked responses in hSkM without impacting hMNS outputs (Supplementary Fig. 5i (middle and right)), further supporting our results. In addition, our results demonstrated projective interconnections between assembled hMNS, forming networks (Fig. 3l). To assess inter-hMNS functional connectivity, we compared two experimental setups: a control group with three hChR2-negative hMNS (hMNS (-)) and an experimental group where only the central neurospheroid expressed hChR2 (hMNS (hChR2+)) while flanking neurospheroids remained hMNS (-). Curare was added before detection to prevent interference from muscle electrical activity. This configuration enabled selective optical activation of the central neurospheroid while monitoring signal transmission to neighboring neurospheroids. Our results showed that the control group exhibited no synchronous spikes following light stimulation, confirming that light exposure itself does not produce non-specific activation. In contrast, the experimental group displayed significant synchronized firing patterns after light stimulation (Fig. 3m, n). Specifically, optogenetic activation of the central hMNS resulted in effective signal transmission to adjacent hMNS, triggering synchronized electrical activity across neurospheroids. Collectively, the electrical activity map provides a simple and practical strategy for functional visualization and readout of neuromuscular in vitro models.

IH-induced functional deficits as an initial response of motor neuron to oxygen deprivation

To investigate the neuromuscular pathological phenotypes driven by IH, we implemented cyclic hypoxia of 1% O_2, based on previously established in vitro IH conditions[24] (Supplementary Fig. 6a). We initially evaluated the impact of IH on MN at early (phase 1, IH p1) and later (phase 2, IH p2) maturation stages (Supplementary Fig. 6b). Motor neurons tend to self-organize into clusters in vitro, influencing both the structural organization and functional integration of neural networks[30]. To this, we replaced low-adhesion plates with Matrigel-coated plates to observe the self-organizing behavior of neurons aggregating from 2D cultures into clusters. We found that exposure to IH (p1) adversely affected the structural integrity of these clusters, resulting in flatter and more irregular formations (Supplementary Fig. 6c), with reductions in diameter and axonal width (Supplementary Fig. 6d–f). The structural mechanical stability of the neural constructs was also compromised during IH (p1) exposure, as shown by the decreased fluorescence expression of NFL and NFH, and a lower NFL/NFH ratio, with no comparable changes observed in the IH (p2) under
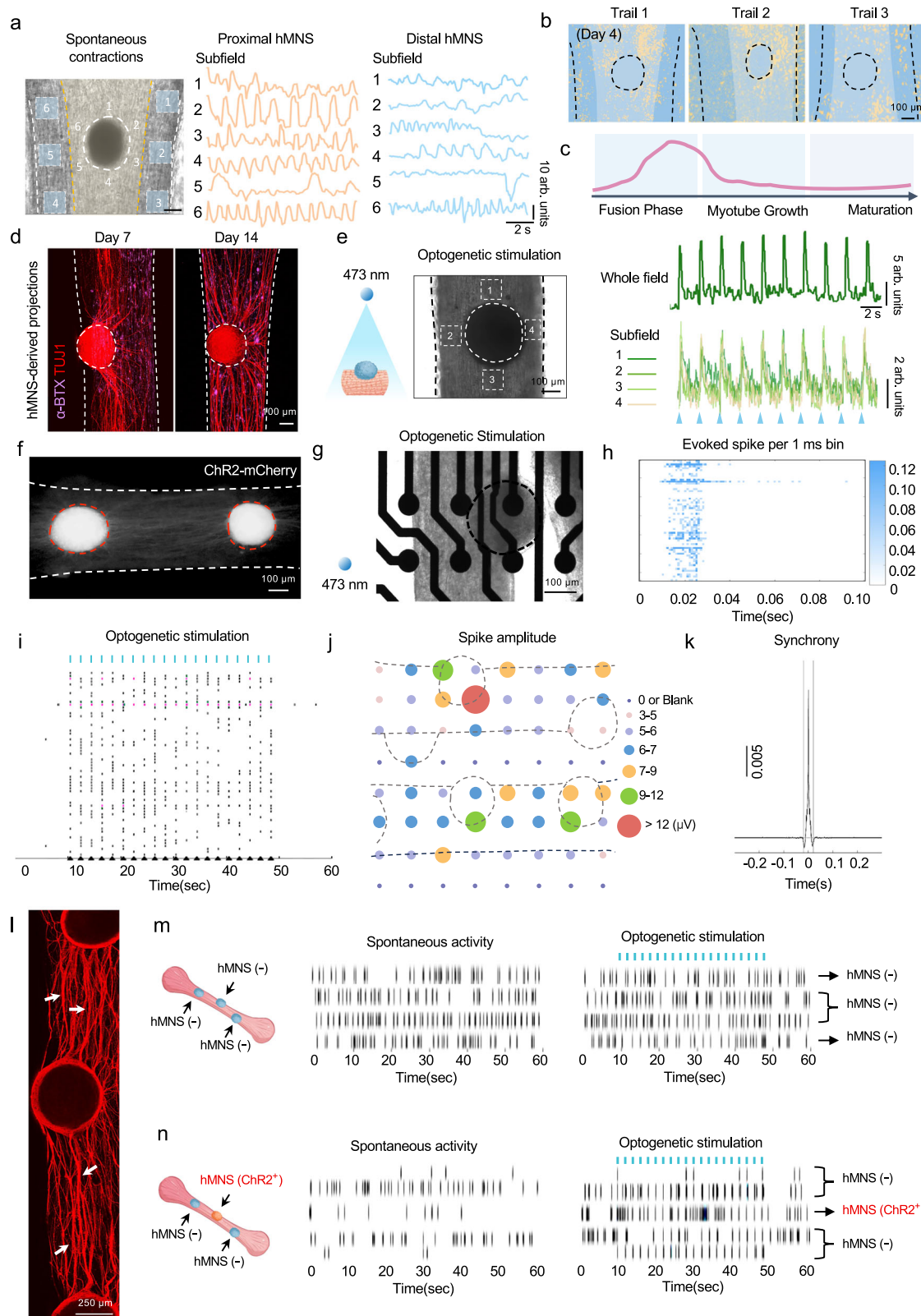
consistent imaging settings (Supplementary Fig. 6g, h). To further explore the specific impact of IH on electrophysiological function, we applied the MEA system to detect spontaneous electrical activity. Interestingly, IH exposure mainly disrupted the early stage of development in phenotypic observations but affected both stages (IH p1 and p2) in functional readouts. The reductions in firing events and amplitudes caused by IH indicated a broad suppression of neuronal

activation (Supplementary Fig. 6i–k), although firing rhythmicity patterns remained unchanged (Supplementary Fig. 6l). These results indicate varying response patterns of MN development stages to IH exposure.

Next, our study focused on hMNS that had reached a phase of self-organization and maturity. Given their advanced and stable functional neuronal characteristics, it is posited that IH exposure (Fig. 4a) could

Fig. 3 | Formation of functional connectivity in motor assembloids.
a Spontaneous contractions in motor assembloids at day 4. Displacement traces in proximal and distal hMNS regions are shown separately for six subfields, depicting distinct contraction patterns over time. Scale bar, 100 μm. **b** Motion analysis maps for spontaneous activity in motor assembloids at day 4 within 10 s. **c** Schematic showing the phase of spontaneous contraction emergence in motor assembloids. **d** Immunofluorescence images of motor assembloids 7 and 14 days post-assembly showing hMNS-derived projections (TUJ1, red; α-BTX, magenta). **e** Motion of motor assembloids under optogenetic stimulation. Setup for optogenetic stimulation of a motor assembloid at 473 nm light (left), with recorded displacement traces from four designated subfields (right). The traces illustrate the contraction responses synchronized with the optogenetic pulses (blue triangles). **f** Representative image of a motor assembloid in which hMNS was transduced with pLenti-hSyn-hChR2(H134R)-mCherry prior to assembly. **g** Bright-field imaging of a motor

assembloid in the microelectrode array (MEA) system. **h** Representative spike time histograms showing the number of spikes evoked per 1 ms bin across a 0.1 s window following stimulation onset. **i** Representative raster plots showing motor assembloid responses to optogenetic stimulation over 1 min (0.5 Hz, 20 ms pulses). Blue ticks signal the optogenetic stimulation pulses. **j** Representative electrical activity mapping of a pair of motor assembloids illustrating variations in mean spike amplitude. **k** Representative neuronal synchrony analysis following stimulation onset. **l** Immunofluorescence images showing axonal projections from motor assembloids. White arrows denote robust axonal connections between hMNS. **m** and **n** Representative raster plots showing spontaneous activity and optogenetic stimulation responses from the control group (**m**) and hMNS (hChR2+) group (**n**) over 1 min. Blue ticks signal the optogenetic stimulation pulses. Three independent experiments was repeated independently with similar results (**d**, **f**, **g**, **l**). Source data are provided as a Source Data file.
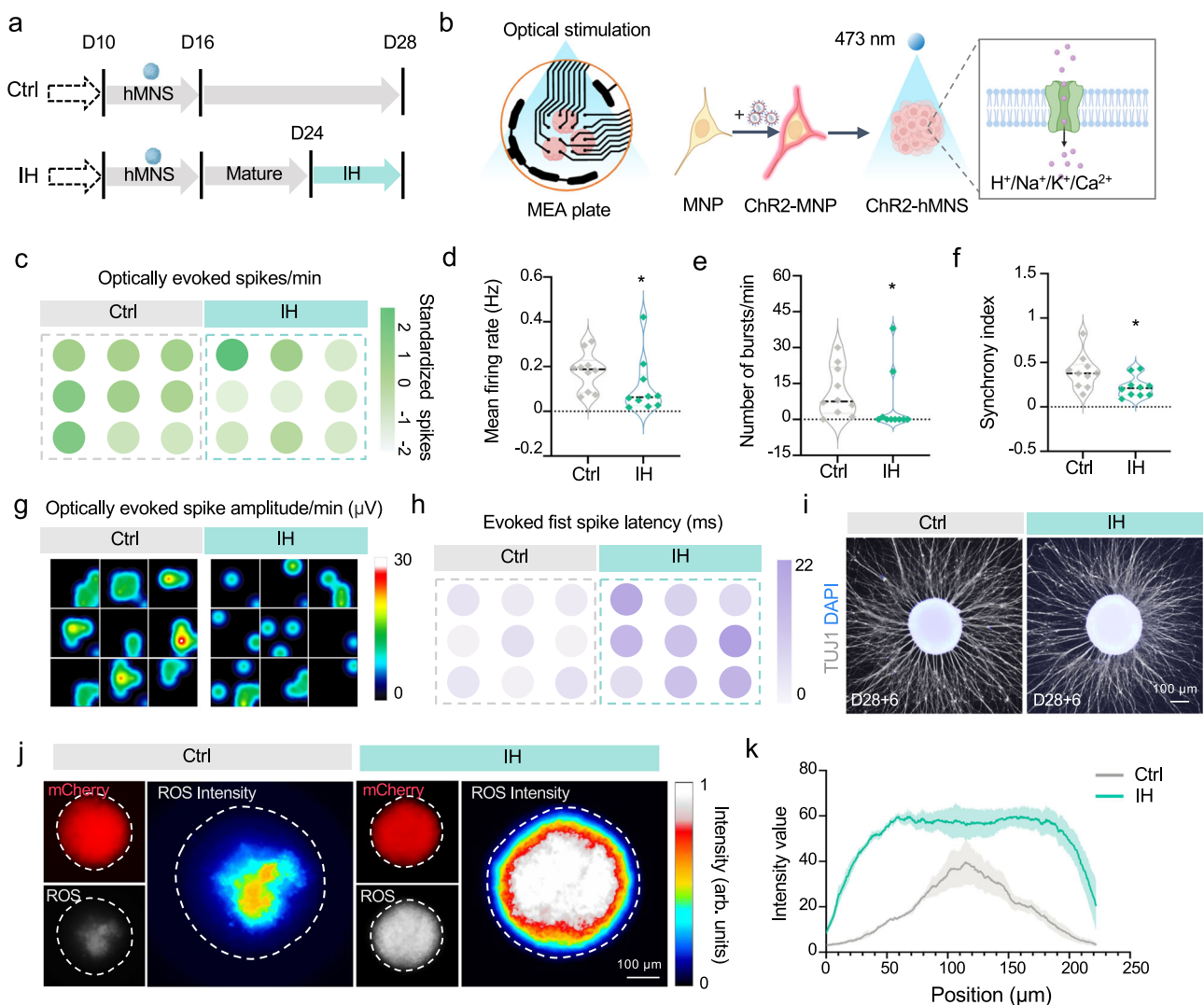
Fig. 4 | Characterization of electrophysiological activity and axonal outgrowth in hMNS exposed to IH. a Timeline for hMNS under normoxia (Ctrl) and intermittent hypoxia (IH), detailing the IH exposure phases. **b** Schematic representation of optogenetic control in an MEA system using ChR2-transfected hMNS to activate ion channels under 473 nm optical stimulation. Created in BioRender. Zhang, W. (2025) https://BioRender.com/z81fuip. **c** Plate maps showing optically evoked spikes per min, with each node representing a well and color intensity indicating standardized spike events. **d**–**f** Quantification of activity parameters, including mean firing rate (**d**), number of bursts per min (**e**), and synchrony index (**f**) from 10 wells (n = 3 hMNS per well). **g** Activity heat maps showing optically evoked spike amplitude (μV), with each map representing a well. **h** Plate map illustrating the time

of first optically evoked spike latency, with each node representing a well and color indicating latency duration. **i** Representative images of hMNS axon growth (TUJ1, gray; nuclei, blue) in Ctrl and IH groups. After formation on D28, including 4 days of IH exposure, hMNS were transferred to a Matrigel-coated dish and cultured for an additional 6 days to visualize neurite elongation. Three independent experiments was repeated independently with similar results. **j** and **k** Representative image (**j**) of reactive oxygen species (ROS) intensity in hMNS exposed to IH, with quantification (**k**) of ROS distribution radially across the spheroids. Data are presented as median with interquartile range. Statistical analysis: **d**, **e**, two-tailed Mann-Whitney test. **f** Two-tailed Student's t test. ***p < 0.001, **p < 0.01, *p < 0.05. Source data are provided as a Source Data file.

lead to impaired neuronal excitability and network synchrony. To investigate this, we manipulated hMNS using optogenetics by introducing ChR2 and activating intracellular ion channels with blue light (0.5 Hz, 10 ms) to control neuronal electrical activity (Fig. 4b). Representative heat maps showed reduced spike amplitudes and fewer optically evoked firing events, while the latency to the first spike was prolonged in the IH condition (Fig. 4c, g, h). Such inhibition of neuronal excitability and response speed has also been detected in patients with hypoxia-related diseases like OSA, implicating pathological involvement of motor neurons[31]. Further analysis revealed that IH exposure downregulated mean firing rate, the number of bursts (events of multiple firing over a short period), and the synchrony index (an indicator of coordinated neuronal firing patterns), which indicated not only reduced individual neuronal activity but compromised network communication and coordination (Fig. 4d–f). However, axonal outgrowth in hMNS, essential for neural network formation, remained unaffected by IH after further culture on Matrigel-coated plates for 6 days (Fig. 4i), pointing to a higher vulnerability in neural function over structure. IH also triggered oxidative stress responses, altering the distribution of reactive oxygen species (ROS) from concentrated central areas to broader regions across the spheroid compared to the Ctrl group (Fig. 4j, k). The accumulation of ROS, reflecting metabolic dysfunction, potentially contributed to the exhaustion of electrically active processes that depend on substantial energy. These findings highlight that the functional deficits triggered by IH may represent an initial response of MN to oxygen deprivation.

The human motor assembloids-on-a-chip as a platform to study neuromuscular pathology in IH-driven disease model through phenotypic and functional readouts

To demonstrate the tractability and the ability of our models to recapitulate human hypoxia-related diseases, we subjected the motor assembloids to the IH environment for 4 days. Morphological analysis initially unveiled that SAA+ multinucleated myofibers in hSkM exhibited coexistent muscle fiber atrophy and hypertrophy with vacuolation compared to the Ctrl group (Fig. 5a). Quantitative analysis of fiber diameters confirmed this heterogeneous response, showing a bimodal distribution where the peak at smaller diameters was more prominent (Supplementary Fig. 7c, d). This pattern means that more myofibers were atrophied and tended to be decompensated. Moreover, the regular and clear striation structure was disrupted after IH exposure (Supplementary Fig. 7e–g). This impaired structural integrity of the myofibres suggested that the NMJ located on these fibers may also be implicated, specifically, a marked reduction in the length of α-BTX-labeled NMJ following IH exposure (Fig. 5a and Supplementary Fig. 7b). For the hMNS part, analysis of axon widths expressing TUJ1 revealed no notable differences between the groups (Fig. 5a and Supplementary Fig. 7a). Subsequent analysis of contractile displacement showed an incremental weakening of function under IH conditions (Fig. 5b). Further evaluation measured the peak amplitude of each waveform and the time taken to reach this peak (Fig. 5c). The results showed a temporal decrease in average contraction peak (Fig. 5d) and a trend where the time to reach the peak was initially shortened and then delayed compared to Ctrl (Fig. 5e), potentially linked to internal rearrangement of myofiber types[10]. Collectively, these findings suggest that IH exposure progressively impairs the contractile functionality of motor assembloids, with the impairment exacerbating over time.

To understand how IH affects the expression of functional proteins related to myofibers and neurofilaments within motor assembloids, we isolated hMNS and their axons from hSkM. In skeletal muscle, slow fibers (type I) are enriched in mitochondria and depend on oxidative phosphorylation (OXPHOS) for sustained activities, whereas fast fibers (type II) primarily utilize glycolysis with lower oxygen demands and are quickly fatigued[32]. During the initial 3 days of IH exposure, expressions of pan-MHC, SAA, and MHC-I remained unchanged, yet a significant reduction occurred by the 4th day. This decline indicated the damage threshold and extensiveness of myofibers under IH, especially in the oxygen-dependent slow fibers. MHC-II protein expression initially increased, reflecting an adaptive rise in glycolytic activity, but decreased by the 4th day due to accumulating IH-induced injury (Fig. 5f and Supplementary Fig. 7h). The IH environment induced a reduction in slow fibers alongside a transient increase in fast fibers, which further explains the dynamic peak times depicted in Fig. 5e. This shift toward a fatigue-prone myofiber composition recapitulates key aspects of the pathology observed in OSA and COPD patients. Furthermore, the response of neurostructural proteins to IH revealed their susceptibility to injury. NFL, essential for axon integrity and conduction velocity, showed a gradual decline in protein expression, underscoring its vulnerability to hypoxic injury. The temporary decline and subsequent recovery of NFM demonstrated adaptability to IH. In contrast, NFH and TUJ1 exhibited resistance to IH, with no significant changes observed throughout the treatment duration (Fig. 5g and Supplementary Fig. 7h).

Next, we characterized the key physiological parameters of motor assembloids using the MEA system. Continuous recordings under IH exposure on the same model (Fig. 5h) showed that organoids lacking PDMS support had slight shape differences within the MEA setup, but their activity remained effectively captured. During IH treatment, electrodes recording hMNS demonstrated a decline in spontaneous electrical activity starting from day 2 and continuing through day 4 (Fig. 5i, j). Optogenetic stimulation still evoked synchronous firing in the motor assembloids, but activity at some electrodes shifted from sustained firing to weakened (Supplementary Fig. 7i, j). Electrical activity mapping further unveiled heterogeneity in firing events between the two functional units within the assembloids (Fig. 5k, l). In particular, under the IH condition, the spike events and amplitude of the hMNS in optogenetically driven motor assembloids were significantly decreased. Meanwhile, hSkM spike events, triggered by hMNS, showed an upward trend, yet the amplitude was also curtailed (Fig. 5m, n). After the cessation of optical stimulation, residual synchronous electrical signals persisted in the neuromuscular system during the buffering period. However, within an additional one-minute recording, the IH group exhibited a reduction in the number of active electrodes involved in single synchronous discharges of motor assembloids (Supplementary Fig. 7k).

Together, the phenotypic and functional readouts of motor assembloids under IH conditions recapitulated neuromuscular pathologies (Fig. 5o), rendering them suitable for developing in vitro models of muscle dysfunction in clinically relevant respiratory disorders. In addition, the suppression of motor neuron firing and the disturbances in their innervated myofibers offer neuro-etiological explanations for neuromuscular interaction deficits that are difficult to detect clinically.

Human motor assembloids-based profiling of hypoxia-driven pathomechanisms and therapeutic attempts targeting NAD+ metabolism

Following the aforementioned results, we further investigated how IH affects the function and metabolism of motor assembloids by bulk RNA sequencing. Initial transcriptomic profiling of the whole motor assembloids identified 545 transcripts induced and 205 transcripts repressed significantly in relation to Ctrl group (Fig. 6a and Supplementary Fig. 8a). KEGG enrichment analysis demonstrated that motor assembloids under IH conditions face metabolic rewiring and survival challenges induced by hypoxic stress (Fig. 6b). Specifically, activation of the HIF-1 signaling pathway directly responded to hypoxia by enhancing glycolysis to provide short-term energy, but prolonged metabolic reprogramming may impair mitochondrial function and intracellular homeostasis[33]. The expression profiles during hypoxic stress were also similar to those observed in COVID-19, suggesting
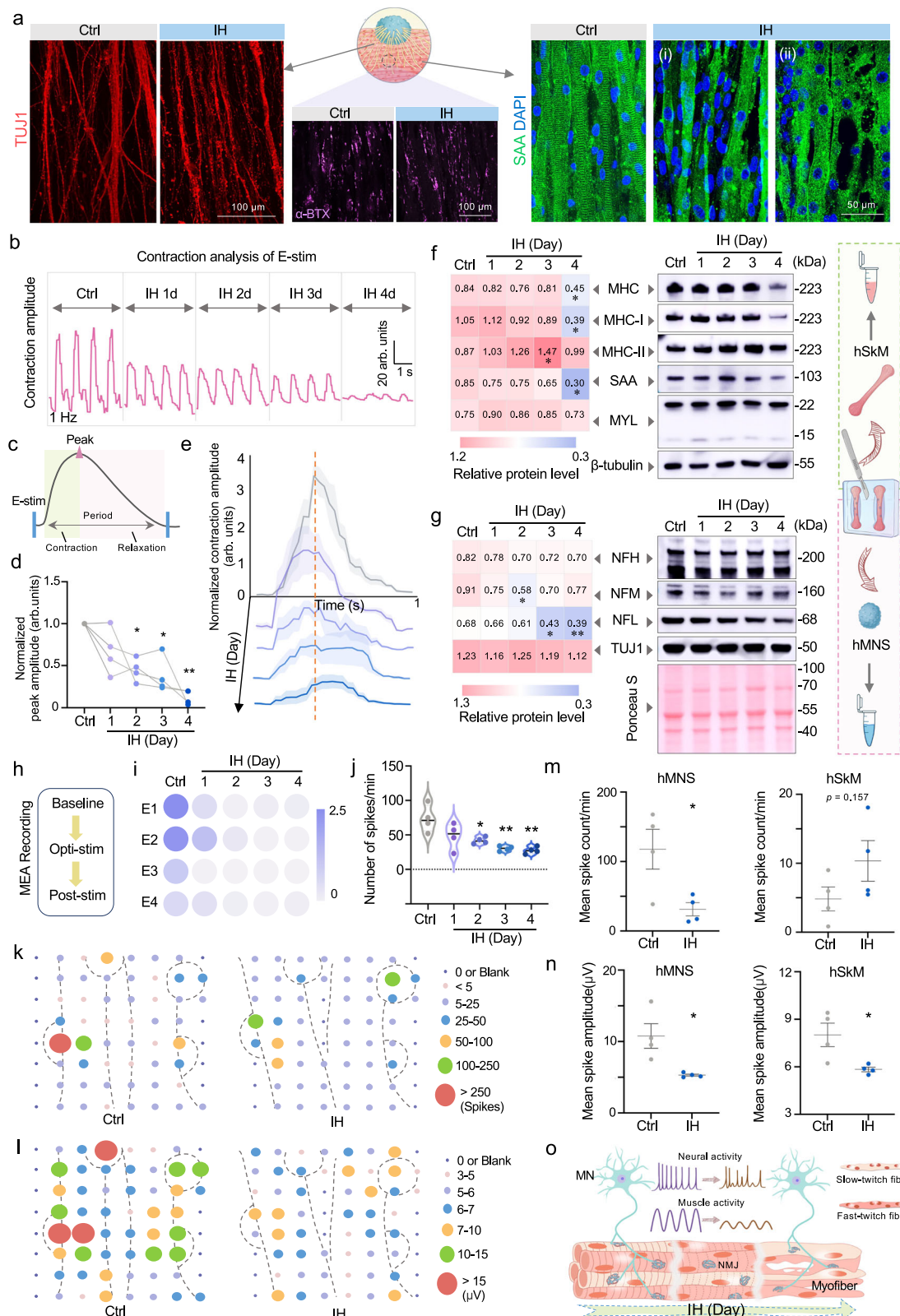
possible shared pathophysiological mechanisms such as inflammation and cell death processes[34,35]. To improve the detection resolution of transcriptomic changes in specific neuromuscular structures, we analyzed localized regions containing hMNS and synaptically innervated hSkM. We observed more pronounced gene expression changes in subfield motor assembloids following IH exposure, with 910 transcripts induced and 982 transcripts repressed (Supplementary Fig. 8b).

GO analysis of differential gene expression revealed enrichment of genes associated with synaptic structure, NMJ function, and ion channel activity (Supplementary Fig. 8c). Moreover, dissection of gene sets in gene set enrichment analysis (GSEA) for "Neuromuscular synaptic transmission" (Fig. 6c) and "Neuromuscular junction" (Supplementary Fig. 8d) identified inhibitory trends. Interestingly, following IH exposure, subfield motor assembloids expressed higher levels

Fig. 5 | Modeling neuromuscular pathology in motor assembloids by IH exposure. a Representative immunofluorescence images for axons (TUJ1; left), AChR clusters (α-BTX; middle), and myofibers (SAA; right) within motor assembloids. **b** Displacement traces depicting contraction amplitudes in motor assembloids under electrical stimulation over 4 days of IH. **c** Schematic detailing the single displacement trace of muscle motion capturing contraction, peak, and relaxation phases in response to electrical stimulation. **d** Quantification of normalized peak amplitude during 4 consecutive days of IH compared to Ctrl. $n = 4$ assembloids. **e** Quantification of a single displacement trace of muscle motion over 4 days of IH, the orange dashed line denotes the peak amplitude of Ctrl. $n = 4$ assembloids. **f** and **g** Representative immunoblots and heatmap profiles showing muscle contractile proteins (**f**) and neurofilament proteins (**g**) over 4 days of IH, with β-tubulin and Ponceau S staining as loading controls, respectively. $n = 3$ independent experiments. **h** Schematic of MEA recording, from baseline, through optogenetic stimulation (opti-stim), to post-optogenetic stimulation (post-stim).

i Plate map of spontaneous mean firing rate (Hz) in hMNS within motor assembloids across 4 days of IH. $n = 4$ assembloids. **j** Quantification of spontaneous spike activity in hMNS within motor assembloids across 4 days of IH. $n = 4$ assembloids. **k** and **l** Representative electrical activity mapping of a pair of motor assembloids illustrating variations in spike events (**k**) and mean spike amplitude (**l**) per min from Ctrl to IH 4 d. **m** and **n** Quantification of electrophysiological parameters, including the mean spike count (**m**) and mean spike amplitude (**n**) per min, recorded from electrodes in hMNS and hSkM regions within motor assembloids across Ctrl and IH 4 d. $n = 4$ assembloids. **o** Schematic overview of the dynamic changes in phenotypic and functional characteristics of motor assembloids in response to IH. Data are presented as mean ± SD (**d**, **f**, **g**, **j**) or ± SEM (**m**, **n**). Statistical analysis: **d** Repeated ANOVA with Tukey multiple comparison. **f**, **g**, **j** One-way ANOVA with Bonferroni multiple comparison. **m**, **n** two-tailed Student's t test. ***$p < 0.001$, **$p < 0.01$, *$p < 0.05$. Source data are provided as a Source Data file.

of genes associated with MN susceptibility and lower levels of genes resistant to MN degeneration (Fig. 6d). Overall, these data further detail and clarify the mechanisms underlying neuromuscular injury induction and response in the motor assembloids IH pathological model.

A key aspect of applying the IH model within the framework of clinical translation is drug discovery and efficacy evaluation. Accordingly, we first screened the top 150 terms demonstrating extensive pathological relevance from the gene expression profile post-IH exposure using GSEA. We then unveiled the overall expression patterns of these terms using clustering networks, allowing us to pinpoint potential drug targets and conduct relevant drug evaluations (Fig. 6e). Clustering network analysis revealed that mitochondrial bioenergetic dysfunction and muscle deficit are prominent features of IH pathology (Fig. 6f and Supplementary Fig. 8e, f). Considering the central role of OXPHOS in cellular energy production and its widespread involvement in the differential gene set, prioritizing OXPHOS repair could improve neuromuscular homeostasis. To validate the transcriptomic findings and target more specific sites, we focused on examining the expression and function of key mitochondrial complex subunit proteins responsible for OXPHOS. Notably, mitochondrial complex I (NADH: ubiquinone oxidoreductase) was significantly inhibited at both mRNA and protein levels, as well as in enzymatic activity (Fig. 6g, h and Supplementary Fig. 8g, h). This dysfunction not only reduced ATP production efficiency but also potentially led to electron retention and leakage in the electron transport chain[36], supported by the widespread increase of ROS level observed in the IH group (Fig. 6i, j). Furthermore, the activity of ATPase/ATP synthase and its subunit (*ATP5B*) mRNA were also inhibited, possibly further exacerbating damage to motor assembloids (Fig. 6h and Supplementary Fig. 8h).

Complex I, the largest component of the electron transport chain, catalyzes the dehydrogenation of NADH to produce NAD^+, a critical coenzyme for mitochondrial energy metabolism and cellular repair[37]. A decline in its activity suggests a disruption of the NAD^+/NADH balance. We found a decrease in NAD^+ levels and a lower NAD^+/NADH ratio following IH exposure (Fig. 6l, m). Although direct therapies for mitochondrial complex I dysfunction are currently unavailable, strategies to replenish NAD^+ represent a feasible approach for recovering energy depletion and repairing cellular damage[38,39]. We considered three key NAD^+ salvage pathways: (i) administering NAD^+ precursors (such as NMN), (ii) activating the rate-limiting enzyme for NAD^+ synthesis (NAMPT agonist NAT), and (iii) inhibiting NAD^+ degradation (CD38 inhibitor 78c), to explore multiple pathways to restore energy balance and reduce oxidative stress (Fig. 6k). These pharmacological treatments, previously applied in sarcopenia[40] and neurodegenerative diseases[41], have not been tested in diseases characterized by IH. Our trials revealed that while NAT had a negligible impact, NMN and 78c differed in their efficacy in restoring NAD^+ levels. Besides increasing NAD^+ levels, 78c corrected the NAD^+/NADH ratio, whereas NMN mainly

restored ATP levels (Fig. 6l–o), demonstrating their respective strengths and limitations in countering the energy and redox imbalances resulting from IH.
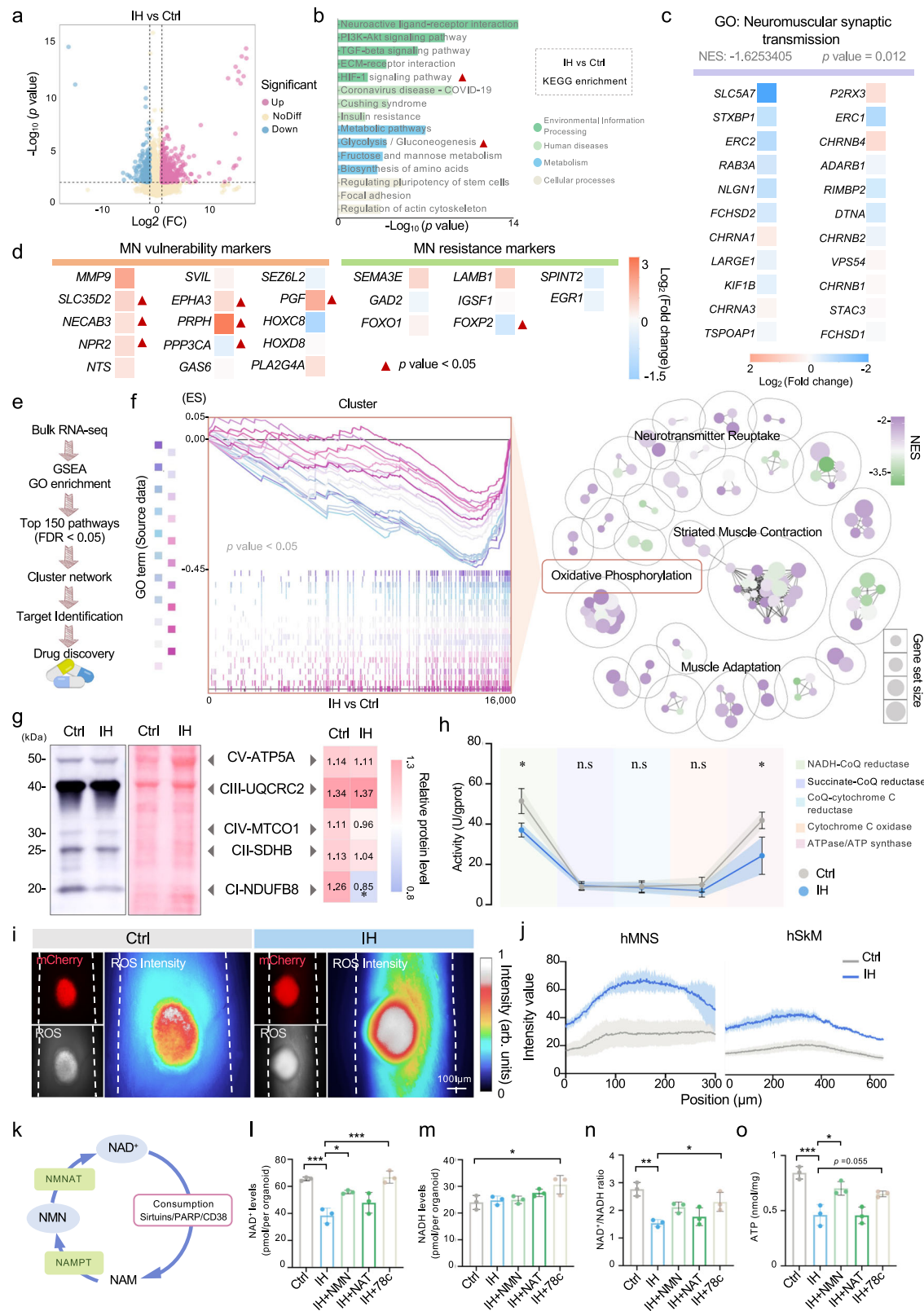
In conclusion, these findings indicate that motor assembloids, serving as a proof-of-concept application, reveal the mechanisms underlying neuromuscular pathology in response to IH disturbance. Moreover, our organoid-based results highlight the potential for targeting the NAD^+ metabolic pathway in treating neuromuscular complications associated with respiratory disorders.

Discussion

We developed an open chip with minimal fabrication requirements to support the self-assembly and long-term culture of anisotropic muscle organoids and motor neuron spheroids. Spatial assembly of motor units on this device establishes functional neuromuscular connections and co-development, which aligns with the broad definition of assembloids[42]. Our research focus was distinct yet complementary to recently reported in vitro neuromuscular models[16,17]. The platform design navigated several physiological integration challenges: (i) an open-chip format that accommodated the cultivation of each functional component while easing neuromuscular functional testing and manipulation; (ii) a patterned layout that enabled surface modifications in specific regions; and (iii) the use of surface modification properties to establish differential tissue adhesion strengths across regions. Indeed, these elements improved the efficiency and stability of subsequent experiments, especially with the introduction of the heterobifunctional crosslinker Sulfo-SANPAH. Initially employed to activate polyacrylamide hydrogel surfaces for enhanced fibroblast adhesion[43], recent applications of Sulfo-SANPAH have included guiding surface-oriented patterning of cell-laden ECM[44]. Therefore, spatial planning of anchoring nodes is essential for skeletal muscle tissues forming linear arrangements. This necessity has led to the prevalent use of dual micropillars in chip systems with dual purposes: stabilization and directional guidance of muscle fiber growth[45,46]. Our findings indicate that devices pretreated with surface modifications achieved a success rate over 90% in forming long-term stable patterned organoids, significantly outperforming the unmodified group. While comparative analysis revealed that other physical fixation methods exhibited comparable performance levels, the surface modification maintained high success rates while demonstrating superior batch-to-batch stability, suggesting its potential value for scalable applications. Furthermore, its attachment-free design offers time savings in device preparation compared to alternative methods.

The stable skeletal muscle architecture establishes a conducive physical microenvironment for hMNS integration. Neuromuscular development involves coordinated neurogenic and myogenic signaling that reciprocally governs differentiation and maturation processes. Our culture observations revealed enhanced spontaneous contractile activity in proximal compared to distal assembly regions. This

differential activity pattern likely results from: (i) shorter axonal distances enabling earlier motor innervation in proximal regions, (ii) higher local neurotrophic factor concentrations from nearby hMNS accelerating NMJ maturation, and (iii) day 5 contractile peaks coinciding with key myoblast fusion, indicating earlier functional connectivity in proximal regions. This spatial pattern aligns with the proximodistal maturation principle observed in vertebrate motor

systems. Many studies on in vitro models have primarily focused on neuron co-culture that enhanced skeletal muscle differentiation[47] and synaptic membrane complexity[27,28], yet studies exploring how skeletal muscle exerted retrograde regulation on motor neuron development are limited. Our research demonstrated that within an in vitro neuromuscular system, the maturation of hSkM not only responded to regulation by hMNS but also promoted the subtype development of

Fig. 6 | Hypoxia-driven pathomechanism profiling in motor assembloids and a transcriptomics-guided drug discovery strategy. a Volcano plot of differential gene expression in whole motor assembloids from IH ($n = 5$ assembloids) and Ctrl ($n = 4$ assembloids). **b** Enrichment of KEGG pathways in whole motor assembloids, focusing on key pathways involved in environmental information processing and metabolism. **c** Heatmap showing the relative changes in gene expression within motor assembloid subfields, based on GSEA analysis of GO terms related to neuromuscular synaptic transmission. **d** Heatmap presenting the relative changes in gene expression of MN vulnerability and resistance markers within motor assembloid subfields, with red triangles indicating significance. **e** Schematic outline of the pathological target identification and drug discovery strategy. **f** Enrichment map and cluster analysis in whole motor assembloids. The network map visualizes the top 150 GSEA GO terms, with GO terms represented as nodes that are connected and clustered into functional themes based on shared gene associations. The functional theme of oxidative phosphorylation (OXPHOS) is highlighted, with the left plot showing all associated GO terms within this cluster. **g** Representative immunoblots (left) and heatmap profiles (right) showing the protein levels of mitochondrial respiratory chain complex subunits in motor assembloids exposed to IH, with Ponceau S staining (total protein) as loading control. $n = 6$ independent experiments. **h** Enzyme activity of mitochondrial complexes I–V in motor assembloids across Ctrl and IH groups. $n = 3$ independent experiments. **i** and **j** Representative image (**i**) of ROS intensity in hMNS exposed to IH, with quantification (**j**) of ROS distribution radially across the spheroids and along the longitudinal diameter of hSkM. **k** Schematic of NAD^+ conversion and consumption in the NAD^+ salvage pathway. **l–n** Quantification of NAD^+, NADH levels, and NAD^+/NADH ratio in motor assembloids. $n = 3$ independent experiments. **o** Quantification of ATP level in motor assembloids. $n = 3$ independent experiments. Data are presented as mean ± SD. Statistical analysis: **g**, two-tailed Student's t test. **h**, two-tailed Student's t test and Mann-Whitney test. **l–o** One-way ANOVA with Bonferroni multiple comparison. ***$p < 0.001$, **$p < 0.01$, *$p < 0.05$. Source data are provided as a Source Data file.

hMNS in return. Moreover, the organized structure of skeletal muscle was helpful for the functional integration of motor neurons[48]. These insights elucidate the bidirectional interaction between hSkM and hMNS during self-organization and can be further investigated into both secretory[49,50] (e.g., cytokines or vesicular interactions) and non-secretory[27] (e.g., neural innervation or mechanical signals) pathways.

Our model also exhibits strong disease modeling potential. Besides identifying typical pathological changes in hSkM, integrating hMNS has also advanced our understanding of the neurogenic damage from IH in muscle dysfunction. Currently, little is known about the direct effects of pathological IH on motor neuron function. First, our studies indicated that functional deficits in hMNS caused by IH preceded structural damage, suggesting an early response to oxygen deprivation stress. Subsequent assessments of hMNS in motor assembloids indicated a reduction in NFL protein expression, a marker potentially indicative of axonal injury in neuromuscular and neurodegenerative disorders[51,52]. In OSA patients, the positive correlation between NFL serum levels and the apnea index[53], commonly attributed to central nervous system issues, but our findings revealed a link between hypoxia and peripheral axonal damage. Lastly, following IH exposure, hMNS displayed higher susceptibility and lower transcription of resistance genes, with diminished electrophysiological activity. This finding provides promising opportunities for developing early neuropathological therapeutic windows for patients with respiratory diseases accompanied by muscle dysfunction.

In addressing neuromuscular assembly damage, we adopted a transcriptomics-based strategy to identify OXPHOS dysfunction as a key pathological mechanism, focusing on NAD^+ metabolism, which is highly sensitive to hypoxia[54]. Previous research showed that disruptions in NAD^+ balance led to neuromuscular degeneration[55]. Supplementing NAD^+ precursors has proven effective in treating conditions like ALS[56], sarcopenia[40], and Parkinson's disease[57] by supporting mitochondrial function and reducing neuromuscular damage. Similarly, in our study, pharmacological interventions targeting three different pathways to salvage NAD^+ exhibited some therapeutic potential. To move these promising treatments to clinical use, it's important to optimize delivery methods, investigate repair mechanisms, and test multi-drug combinations in preclinical models.

This study presents certain limitations that merit further exploration. First, like many other 3D neuromuscular models[17,58], our study encountered restricted penetration and distribution of axons in deeper muscle tissues. While these models do not entirely replicate the precise innervation patterns observed in vivo, they still effectively capture essential aspects of neuromuscular interactions. This is partly due to: (i) potential signaling molecule crosstalk between neurons and muscle cells; (ii) motor neuron stimulation may induce contractions in non-innervated muscle fibers, likely driven by ion channel and calcium ion activity cascades. In addition, the MEA designed for monolayer cultures offers limited recording in 3D organoids, leaving some electrophysiological activities undetected. Future efforts will focus on enhancing detection through compatible 3D MEA technologies.

In conclusion, our study presents a geometric constraint-driven approach for constructing organized human motor assembloids-on-a-chip through simple surface modification. This platform provides physiologically relevant neuromuscular phenotypes and reliable functional readouts. In disease modeling applications, assembloids exposed to IH recapitulated clinically relevant pathological phenotypes and effectively captured pathodynamic features of the human neuromuscular system. Furthermore, when combined with mechanistic investigations and drug discovery, this platform demonstrates promising translational potential. Thus, the framework developed in this study serves as a tool for hypothesis testing and mechanism elucidation, supplementing current preclinical neuromuscular research methods. Building upon this in vitro model, the development of more extensive organoid systems will broaden the horizons of pathophysiological research, thereby enhancing understanding into the simulation of tissue morphogenesis or complex multi-organ interactions.

Methods

Human motor assembloids device fabrication

The human motor assembloids device was designed employing CAD software (SolidWorks, Dassault Systèmes SolidWorks Corporation) and 3D machined from a polytetrafluoroethylene (PTFE) master mold, composed of a square base and two patterned solid columns atop. For device fabrication, PDMS mixture (PDMS base and curing agent mixed at a 10:1 weight ratio) was poured into culture plates such that the master within was submerged at least 2 mm. After degassing, the mixture was cured at 70 °C for 2 h. The molded PDMS device was then removed from the master and revealed two 3D culture chambers with the top openings, each incorporating a body and two anchor nodes. Prior to use, all devices were sterilized by ultraviolet (UV) light for at least 90 min.

Region-specific surface modification

To form a 3D organoid model, region-specific surface modification was conducted on the PDMS device. The body area of the device was coated with 0.2% Pluronic® F-127 (Sigma-Aldrich, P2443) solution and kept at room temperature for at least 45 min to prevent nonspecific tissue adhesion. This solution was introduced incrementally to avoid spillage into the anchor nodes on either side. For the generation of an anisotropically constrained skeletal muscle bundle, the surface functionalization of the anchor nodes was performed using Sulfo-SANPAH. Sulfo-SANPAH (Sigma-Aldrich, 803332) was dissolved in deionized water to a stock concentration of 50 mg/mL, and then 1:50 diluted for a working concentration when used[44]. Sulfo-SANPAH was pipetted into

the anchor nodes of the device, leaving approximately 1 mm of dry area on the PDMS surface between the Pluronic® F-127 solution and Sulfo-SANPAH droplets. The surface tension effects allowed both to be selectively retained in their respective regions without intermingling. Subsequently, the devices were exposed to UV light at 365 nm for 6 min, during which the Sulfo-SANPAH darkened. Two-thirds of the Sulfo-SANPAH droplets were then aspirated, with the remaining portion being subjected to another UV exposure for 6 min. Following the Sulfo-SANPAH treatment, the devices were rinsed three times with PBS. Cell seeding was promptly conducted within 3–5 min due to the challenge of sustaining long-term surface functionalization.

Cell culture

hiPSCs. The hiPSCs used in this study were purchased from Cell Bank/Stem Cell Bank, Chinese Academy of Sciences (DYR0100). The undifferentiated hiPSCs were maintained on Matrigel (Corning, 354277)-coated plates and fed daily with Essential 8 medium (Gibco, A1517001) or ncTarget hPSC medium (Nuwacell Biotechnology CO., Ltd, RP01020). The cells were passaged using 0.5 mM EDTA (Nuwacell Biotechnology CO., Ltd, RP01007) about every 3 days and re-plated at a density of 1×10^5 cells/well in expansion medium containing 2.5 μM Blebbistatin (Nuwacell Biotechnology CO., Ltd, RP01008) for 24 h. After multiple passages, all cell lines were examined for a normal karyotype.

hSkM cells and Mouse myoblasts (C2C12). hSkM cells were purchased from the Lifeline® Cell Technology (FC-0091). hSkM cells were expanded in StemLife Sk Medium Complete kit (Lifeline® Cell Technology, LL-0069) and passaged using 0.25% Trypsin-EDTA (Biosharp, BL512A) when they reached ~70% confluency. Subsequent experiments employed passages 3–6. For mouse myoblasts, C2C12 (purchased by Cell Bank/Stem Cell Bank, Chinese Academy of Sciences, SCSP-505) were cultured in DMEM (VivaCell Biosciences, C3113-500) supplemented with 10% fetal bovine serum (FBS, Gibco) and 1% penicillin/streptomycin (Biosharp, BL505A). C2C12 was only used in the formation test of myobundles shown in Supplementary Fig. 2e.

All cells were kept in humidified incubators at 37 °C and 5% CO_2.

Generation of hMNS from hiPSCs

The generation of hMNS from hiPSCs was performed using an established protocol with some modifications[59]. In detail, on day −1, hiPS cell colonies were dissociated into single cells with Accutase, re-plated at a density of 3×10^5 cells/well in 6-well plates coated with Matrigel. Cells were cultured in neural medium containing DMEM/F-12 (Gibco, 11320033), Neurobasal-A (Gibco, 10888022) at 1:1, B-27 plus (1:100, Gibco, A3582801), N-2 (1:200, Gibco, 17502048), 0.1 mM L-Ascorbic Acid (Sigma-Aldrich, A4544), GlutaMax (1:100, Gibco, 35050061), 0.5% penicillin/streptomycin and supplemented with 10 μM Blebbistatin, 3 μM CHIR-99021 (MedChemExpress, 10182B), 2 μM DMH-1 (MedChemExpress, 12273), and 2 μM SB-431542 (MedChemExpress, 10431). On day 0, medium was replaced without Blebbistatin and cells were cultured for 5 additional days to induce NEP cells with daily medium changes. From day 5–10, NEP cells were transferred to neural medium supplemented with 1 μM CHIR-99021, 2 μM DMH-1, 2 μM SB-431542, 0.1 μM Retinoic acid (RA, Sigma-Aldrich, R2625) and 0.5 μM Purmorphamine (Selleck, S3042). The medium was changed every day until NEP differentiated into MNPs on day 10. From day 10–16, the MNPs were dissociated and transferred into ultra-low attachment 96-well plates (PrimeSurface, MS-9096VZ) in neural medium supplemented with 0.5 μM RA and 0.1 μM Purmorphamine. From day 16 onward, neural medium was supplemented with 0.5 μM RA and 0.1 μM Purmorphamine, 5 μM DAPT (Selleck, S2215), 20 ng/mL BDNF (Peprotech, 450-02) and 20 ng/mL GDNF (Peprotech, 450-10) every other day. A schematic detailing the hMNS formation was shown in Supplementary Fig. 1a.

Generation of human motor assembloids in defined device

Region-specific surface modification of the PDMS device was performed before cell seeding, as described in the above section, and the subsequent procedure was completed within the specified timeframe. 3D human skeletal muscle tissues were generated in culture using the reagents as previously reported[29]. In detail, for two myobundles in a device, hSkM cells were dissociated and resuspended at a density of 1.5×10^6 cells in 21.5 μL medium containing 1.5 μL of 100 U/mL thrombin (Sigma-Aldrich, T4648) and 0.5 μL of 10 mg/mL aprotinin (Sigma-Aldrich, A1153) as a cell mixture. Concurrently, a separate hydrogel mixture was prepared, which contained 15 μL of 20 mg/mL fibrinogen (Sigma-Aldrich, F8630), 15 μL of Matrigel (Corning, 354234) and 15 μL of medium. Both the cell and hydrogel mixtures were maintained in an ice bath until thoroughly mixed prior to use. The cell-laden hydrogel was immediately loaded into the modified PDMS device. After 2 min of polymerization, hMNS (250 ± 50 μm) were seeded on the surface of the gelled hSkM culture at a density of 3-4 per myobundle, evenly distributed along the length of the myobundle main body. The device was then incubated at 37 °C for 1.5 h to ensure complete polymerization. The hSkM cells growth medium, containing 10 ng/mL BDNF, 10 ng/mL GDNF and 1.5 mg/mL 6-aminocaproic acid (Sigma-Aldrich, A7824), was added for 2 days of culture. The growth medium was aspirated, followed by meticulous incisions along the PDMS borders on either side of the body area with a scalpel to remove adherent cultures while ensuring the anchor nodes were not disrupted. Subsequently, human motor assembloids were maintained in DMEM supplemented with 2% horse serum (Hyclone, SH30074.03), 10 ng/mL BDNF, 10 ng/mL GDNF, 2 mg/mL 6-aminocaproic acid, and 1% penicillin/streptomycin for maturation and assembly. The culture medium was refreshed every other day.

Intermittent hypoxia protocol

In the pathological model, cells/spheroid/assembloids were kept in sub-chambers of an incubator, which were attached to an external computer-driven gas controller (BioSpherix, OxyCyler C42, Redfield, NY, USA). This system can regulate the inflow of O_2/N_2 to generate periodic changes in O_2 concentration based on pre-set dynamic oxygen profiles. For the IH profile, O_2 cycle was set at 1% for 40 min followed by 21% for 20 min, with CO_2 maintained at 5% (Supplementary Fig. 6a). The control group was cultured in normoxia (21% O_2 and 5% CO_2) for equivalent durations.

ROS imaging and assessment

To assess the level of ROS within the spheroid, MNS were incubated with 10 μM DCFH-DA (Beyotime, S0033S) for 30 min at 37 °C, followed by three times washes with DMEM/F-12 medium. A Leica DMi8 microscope was utilized for ROS fluorescence imaging. The acquired images were subsequently analyzed for ROS localization and fluorescence intensity using the NIH ImageJ (version 2.9.0; FIJI) software.

Quantification of NAD⁺/NADH levels

The NAD^+/NADH levels were quantified using a commercial kit (Sigma-Aldrich, MAK037) as per the manufacturer's protocol. The spheroid or assembloids were harvested and rinsed with cold PBS before lysis in the NAD^+/NADH extraction buffer. After low-temperature centrifugation, the supernatant was divided into two parts. For NADH detection only, one portion of the supernatant was heated at 60 °C for 30 min to decompose NAD^+ before reaction. For total NAD detection, the other portion of the supernatant was kept on ice. Subsequently, all samples were added to a 96-well plate and incubated with the reaction mix for 5 min at room temperature. Following the addition of NADH developer, the absorbance of the samples in the plate was measured at 450 nm after 1-2 h. Finally, the amount of NAD_{total} and NADH were calculated through a standard curve, and the ratio of NAD^+/NADH was determined as $(NAD_{total}-NADH)/NADH$.

ATP detection

ATP levels were determined using a commercial ATP detection kit (Sigma-Aldrich, MAK190). Fresh assembloid samples were homogenized with 100 μL lysis buffer using a tissue homogenizer. Following centrifugation at 12,000 r/min for 5 min at 4 °C, the resulting supernatants were transferred to 96-well plates containing 50 μL ATP detection reagent. ATP concentrations were quantified using luminometry.

Immunofluorescence staining protocol

The hMNS were fixed in 4% paraformaldehyde (PFA, Solarbio, P1110) at room temperature for 30 min, while human motor assembloids were fixed in 2% PFA overnight at 4 °C. Fixation was followed by three washes with PBS, and incubation in blocking solution containing 5% donkey serum and 0.3% Triton X-100 in PBS overnight at 4 °C. Over the following two days, the samples were sequentially incubated overnight at 4 °C with primary antibodies in blocking/permeabilization solution, followed by secondary antibodies at 4 °C overnight in the dark after washing three times (Supplementary Data 1 shows all antibodies information and dilution in this study). After additional washes with PBS, samples were counterstained with DAPI (Beyotime, C1006) for nuclei visualization. Finally, samples were mounted on glass microscope slides and imaged on an Olympus FV3000 laser scanning microscope or Leica DMi8 microscope. All images were processed with NIH ImageJ and Adobe Photoshop (version 26.0.0).

Glutamate uncaging and electrical field stimulation

The intact assembloids, still in the PDMS device, were visualized in the microscope using a 10x objective. For glutamate uncaging experiments, MNI-caged-L-glutamate (Tocris, 1490) was applied at a concentration of 5 mM in culture medium. Optical stimulation was performed with a 405 nm light to uncage glutamate. For electrical field stimulation, a custom-made 6-well plate containing electrodes was used after sterilization by UV light. Copper wires welded to the electrodes were hooked up to a commercial power amplifier (Aigtek, ATA-304). A digital oscilloscope (Rigol, DG1022Z) was used to confirm the frequency and amplitude of signals before connecting the power amplifier to the copper wires. The samples were placed in the Tyrode's buffer within the stimulation plate and then stimulated using square pulses with 20 V and the reported frequencies.

Optogenetic manipulation of hMNS

hiPSCs-derived MNPs were subjected to viral transduction with either pLenti-eSyn-hChR2 (H134R)-eGFP-WPRE-pA or pLenti-hSyn-hChR2 (H134R)-mCherry-ER2-WPRE-pA (LTR), both recombinant lentiviruses provided by Shanghai Taitool Bioscience Co., Ltd., China, for the expression of a mutated variant of the light-sensitive ion channel channelrhodopsin-2H134R. The MNPs were seeded at a density of 2×10^5 cells/well on a Matrigel-coated 6-well plate and incubated in MNPs expansion medium containing 10 μM Blebbistatin. After 24 h, the medium was replaced with Blebbistatin-free MNPs expansion medium. The lentiviral vector containing the respective plasmid was then added at the optimal multiplicity of infection (MOI = 20), along with the HitransG A viral transfection reagent (Shanghai GeneChem-Technology Co., Ltd, REV004). The medium was refreshed at 24 h post-transfection. In fluorescence staining studies, cells expressing either GFP or mCherry were stained with dyes of a color distinct from their own fluorescence to avoid overlap.

Microelectrode array (MEA) monitoring and analysis

The hMNS and whole assembloids were transferred to a 24-well (16 electrodes per well) and 6-well (64 electrodes per well) MEA plate (Axion BioSystems), respectively, prior to recording. For recording the electrophysiological activity of hMNS, the hMNS were seeded onto the electrode grid of Matrigel-coated plates. The medium was removed until only a thin layer remained to promote attachment of hMNS, with each well then supplemented with 500 μL medium after incubating at 37 °C for 1 h. For recording spontaneous and evoked responses in human motor assembloids, the neurons and skeletal muscle fibers within the assembloids need to be in contact with the electrodes on the MEA plate. When preparing samples for electrophysiological detection, the hMNS were seeded on hSkM in a compact arrangement to better match the electrode array coverage and enhance the acquisition of valid electrophysiological data. Prior to recording, the assembloids were removed from the device and then immediately transferred into the electrode grid of the inner well. A hydrogel mixture consisting of Matrigel, fibrinogen and medium in equal parts was prepared. After adding thrombin, the mixture was applied around the assembloids to promote adhesion. The plates were left at 37 °C for the hydrogel to solidify over the assembloids. After 2 h, 1.5 mL maturation medium was added slowly to each well.

The electrophysiological activity of samples was recorded in a Maestro Pro MEA system and AxIS Navigator software (Axion BioSystems) under environmentally controlled conditions (37 °C, 5%CO_2). Data was acquired at a sampling frequency of 12.5 kHz with a digital bandpass filter (200–3000 Hz for Spikes setting and 1–2000 Hz for Field Potentials setting). Neural spikes were identified as peaks in voltage surpassing $6 \times$ standard deviation on each electrode. Optogenetic stimulation was performed with the Lumos (Axion Biosystems) using 475 nm light at 0.5 Hz. Spike data was processed further, and statistics generated using the Axion Neural Metric Tool (Axion Biosystems).

Real-time quantitative PCR

Total RNA was isolated using the conventional procedure with TRIzol reagent (Invitrogen, 15596018), chloroform and isopropanol. The concentration and purity of each RNA sample were assessed by NanoDrop One (Thermo Fisher Scientific). Reverse transcription of 500 ng RNA was then conducted using a Fast Quant RT Kit with gDNase (Tiangen, KR106) to prepare cDNA. The cDNA was used as a template for a real-time quantitative PCR (qPCR) assay performed using SuperReal PreMix Plus-SYBR green (Tiangen, FP205) according to the manufacturer's instructions. Relative mRNA expression was calculated using the ΔΔCt method and normalized by GAPDH or 18S. All primer sequences used are listed in Supplementary Data 1.

RNA sequencing (RNA-seq) and transcriptomic analysis

To profile the transcriptomic information of human motor assembloids, the RNA-sequencing workflow was facilitated by LC-BioTechnology Co., Ltd. (Hangzhou, China). Briefly, the human motor assembloids from different treatment groups were processed with TRIzol reagent. Messenger RNAs (mRNAs) were enriched and isolated from the total RNA using oligo (dT) magnetic beads and subsequently fragmented in the fragmentation buffer. The resultant short fragments served as templates for the synthesis of first-strand cDNA using SuperScript™ II Reverse Transcriptase. Following the addition of U-labels to the second-stranded DNAs, the heat-labile UDG enzyme was used for post-treatment. A-base additions prepared the fragments for adapter ligation, and PCR amplification followed, yielding a cDNA library. Finally, sequencing of the samples was performed using PE150 on the Illumina Novaseq™ 6000. For motor neuron transcriptomic analysis, we mechanically separated hMNS from the assembloid cultures. After PBS washing and transfer to clean dishes, assembloids were examined under a stereomicroscope. Using sterile surgical blades, hMNS tissue was gently scraped from the hSkM surface, with collection areas extending beyond the neurospheroid perimeter to include adjacent hSkM surface regions. This approach captured genes expressed in axonal projections and synaptic interfaces.

For bioinformatics analysis, read cleaning and quality checks were conducted using fastp software, followed by alignment of the reads to the Homo sapiens (GRCh38) reference genome through HISAT2. Subsequently, StringTie was employed for transcriptome reconstruction and abundance estimation. Differential expression analysis was carried out by the R package DESeq2, using a fold change threshold of > 2 or < 0.5 and $p < 0.05$ from a parametric F-test comparing nested linear models.

Immunoblotting

The samples were homogenized in cold RIPA buffer (Beyotime, P0013B) supplemented with protease/phosphatase inhibitor cocktail (Cell Signaling Technology, 5872), after which the total protein concentration was quantified using the BCA Protein Assay Kit (Thermo Fisher Scientific, 23225). The protein lysates were then denatured with SDS loading buffer and boiled at 98 °C for 10 min, before loading onto 4–12% Precast Gel (Tanon, 180-9115H). Following separation, the proteins were transferred onto polyvinylidene fluoride membranes using an electrophoresis and blotting system (Bio-Rad, 1658033). The membrane was stained with Ponceau S (Solarbio, P0012) to visualize total protein loading, and the image was captured to record. After rinsing the membranes until destained, they were blocked with 5% skim milk in 1 × TBST (Solarbio, T1082) buffer for 1 h at room temperature. Subsequently, the membranes were incubated with primary antibodies at 4 °C overnight, followed by washing three times and an incubation with HRP-conjugated secondary antibodies at room temperature for 1.5 h. All antibody information and dilutions were listed in Supplementary Data 1. Finally, blots were developed with the ECL Western Blotting Substrate (Thermo Fisher Scientific, 34580), and images were acquired using the Amersham Imager 600 system (GE Healthcare). Signal intensities were analyzed by NIH ImageJ.

Contraction characteristics analysis

The automated, open-source ImageJ plugin MUSCLEMOTION was utilized to quantify skeletal muscle contraction[60]. MUSCLEMOTION provides a reliable methodology for measuring contraction dynamics by assessing the cumulative absolute variations in pixel intensity between a selected reference frame and the target frame (imgtar - imgref = imgresult). During the analysis of spontaneous contractions in skeletal muscle, the simultaneous movement of muscle fibers in different directions across various areas could potentially result in an unchanged sum of pixel intensities. To capture an authentic representation of movement, a strategy was devised whereby the imaging field was segregated into multiple subfields, with each subjected to separate analysis. In our model, an orderly arrangement of muscle fibers upon the maturation of the skeletal muscles was observed. Following electrical stimulation, a predominantly consistent direction of movement was observed, which was then selected for comprehensive analysis across the entire assembloid. The subsequent task involved calculating the displacement of the skeletal muscle systematically, adhering to the previously outlined procedure by MUSCLEMOTION.

Statistical analysis

Statistical analysis was conducted using the GraphPad Prism software (version 10.4.1). Replicates typically refer to independent experiments or individual samples, while the technical replicates are explicitly mentioned in the figure legend. Data were assessed for normality and variance according to the type of experiment. For normally distributed data, an unpaired t test (for two groups) or one-way/two-way ANOVA with Bonferroni post hoc test (for multiple groups) was applied, and results are presented as the means ± SD or SEM as specified in each figure legend. Alternatively, non-parametric data analysis involved the Mann-Whitney test for two groups and the Kruskal-Wallis with post hoc Dunn's test for multiple comparisons, and results were expressed as median with quartiles, unless noted otherwise. Data are considered at $p < 0.05$ as statistically significant.

Reporting summary

Further information on research design is available in the Nature Portfolio Reporting Summary linked to this article.

References

1. Rangaraju, V., Calloway, N. & Ryan, T. A. Activity-driven local ATP synthesis is required for synaptic function. *Cell* **156**, 825–835 (2014).
2. Lv, R. et al. Pathophysiological mechanisms and therapeutic approaches in obstructive sleep apnea syndrome. *Signal Transduct. Target. Ther.* **8**, 218 (2023).
3. Prabhakar, N. R., Peng, Y. J. & Nanduri, J. Hypoxia-inducible factors and obstructive sleep apnea. *J. Clin. Invest.* **130**, 5042–5051 (2020).
4. Attaway, A. H. et al. Adaptive exhaustion during prolonged intermittent hypoxia causes dysregulated skeletal muscle protein homeostasis. *J. Physiol.* **601**, 567–606 (2023).
5. Dunican, E. M. et al. Mucus plugs and emphysema in the pathophysiology of airflow obstruction and hypoxemia in smokers. *Am. J. Respir. Crit. Care Med.* **203**, 957–968 (2021).
6. Serebrovska, Z. O. et al. Hypoxia, HIF-1α, and COVID-19: from pathogenic factors to potential therapeutic targets. *Acta Pharmacol. Sin.* **41**, 1539–1546 (2020).
7. Lavie, L. Oxidative stress in obstructive sleep apnea and intermittent hypoxia—revisited—the bad, ugly, and good: implications to the heart and brain. *Sleep. Med. Rev.* **20**, 27–45 (2015).
8. Maltais, F. et al. An official American Thoracic Society/European Respiratory Society statement: update on limb muscle dysfunction in chronic obstructive pulmonary disease. *Am. J. Respir. Crit. Care Med.* **189**, e15–e62 (2014).
9. Tao, X. et al. Obstructive sleep apnea (OSA) is associated with increased risk of early-onset sarcopenia and sarcopenic obesity: results from NHANES 2015-2018. *Int. J. Obes.* **48**, 891–899 (2024).
10. Sepúlveda-Loyola, W. et al. Diagnosis, prevalence, and clinical impact of sarcopenia in COPD: a systematic review and meta-analysis. *J. Cachexia Sarcopenia Muscle* **11**, 1164–1176 (2020).
11. Sériès, F. J., Simoneau, S. A., St Pierre, S. & Marc, I. Characteristics of the genioglossus and musculus uvulae in sleep apnea hypopnea syndrome and in snorers. *Am. J. Respir. Crit. Care Med.* **153**, 1870–1874 (1996).
12. Smirne, S. et al. Muscle fibre type and habitual snoring. *Lancet* **337**, 597–599 (1991).
13. Beaumont, M. et al. Effects of inspiratory muscle training on dyspnoea in severe COPD patients during pulmonary rehabilitation: controlled randomised trial. *Eur. Respir. J.* **51**, 1701107 (2018).
14. Eckert, D. J. Phenotypic approaches to obstructive sleep apnoea—new pathways for targeted therapy. *Sleep. Med. Rev.* **37**, 45–59 (2018).
15. Clevers, H. Modeling development and disease with organoids. *Cell* **165**, 1586–1597 (2016).
16. Faustino Martins, J. M. et al. Self-organizing 3D human trunk neuromuscular organoids. *Cell Stem Cell* **26**, 172–186.e6 (2020).
17. Andersen, J. et al. Generation of functional human 3D cortico-motor assembloids. *Cell* **183**, 1913–1929.e26 (2020).
18. Hofer, M. & Lutolf, M. P. Engineering organoids. *Nat. Rev. Mater.* **6**, 402–420 (2021).

19. Scheel, M. et al. Diffusion tensor imaging of skeletal muscle—correlation of fractional anisotropy to muscle power. *Rofo* **185**, 857–861 (2013).

20. Shimizu, K. et al. Alignment of skeletal muscle cells facilitates acetylcholine receptor clustering and neuromuscular junction formation with co-cultured human iPSC-derived motor neurons. *Cells* **11**, 3760 (2022).

21. Hofemeier, A. D. et al. Global and local tension measurements in biomimetic skeletal muscle tissues reveals early mechanical homeostasis. *ELife* **10**, e60145 (2021).

22. Ostrovidov, S. et al. 3D bioprinting in skeletal muscle tissue engineering. *Small* **15**, e1805530 (2019).

23. Jana, S., Levengood, S. K. & Zhang, M. Anisotropic materials for skeletal-muscle-tissue engineering. *Adv. Mater.* **28**, 10588–10612 (2016).

24. Li, J. et al. An engineered anisotropic skeletal muscle organoid-on-a-chip for deciphering muscle response under intermittent hypoxia. *Adv. Funct. Mater.* **34**, 2401564 (2024).

25. Buchner, F., Dokuzluoglu, Z., Grass, T. & Rodriguez-Muela, N. Spinal cord organoids to study motor neuron development and disease. *Life* **13**, 1254 (2023).

26. Sunadome, K. et al. Directionality of developing skeletal muscles is set by mechanical forces. *Nat. Commun.* **14**, 3060 (2023).

27. Kim, J. H. et al. Neural cell integration into 3D bioprinted skeletal muscle constructs accelerates restoration of muscle function. *Nat. Commun.* **11**, 1025 (2020).

28. Das, S. et al. Motor neurons and endothelial cells additively promote development and fusion of human iPSC-derived skeletal myocytes. *Skelet. Muscle* **14**, 5 (2024).

29. Madden, L. et al. Bioengineered human myobundles mimic clinical responses of skeletal muscle to drugs. *ELife* **4**, e04885 (2015).

30. Hörberg, C. J. et al. Spontaneous cell cluster formation in human iPSC-derived neuronal spheroid networks influences network activity. *eNeuro* https://doi.org/10.1523/eneuro.0143-22.2022 (2022).

31. Saboisky, J. P. et al. Neurogenic changes in the upper airway of patients with obstructive sleep apnea. *Am. J. Respir. Crit. Care Med.* **185**, 322–329 (2012).

32. Qaisar, R., Bhaskaran, S. & Van Remmen, H. Muscle fiber type diversification during exercise and regeneration. *Free Radic. Biol. Med.* **98**, 56–67 (2016).

33. Miyata, T., Takizawa, S. & van Ypersele de Strihou, C. Hypoxia 1. Intracellular sensors for oxygen and oxidative stress: novel therapeutic targets. *Am. J. Physiol. Cell Physiol.* **300**, C226–C231 (2011).

34. Wang, Y. & Perlman, S. COVID-19: inflammatory profile. *Annu. Rev. Med.* **73**, 65–80 (2022).

35. Qiu, B. et al. Fatal COVID-19 pulmonary disease involves ferroptosis. *Nat. Commun.* **15**, 3816 (2024).

36. Okoye, C. N., Koren, S. A. & Wojtovich, A. P. Mitochondrial complex I ROS production and redox signaling in hypoxia. *Redox Biol.* **67**, 102926 (2023).

37. Fiedorczuk, K. et al. Atomic structure of the entire mammalian mitochondrial complex I. *Nature* **538**, 406–410 (2016).

38. McElroy, G. S. et al. NAD+ regeneration rescues lifespan, but not ataxia, in a mouse model of brain mitochondrial complex I dysfunction. *Cell Metab.* **32**, 301–308.e6 (2020).

39. Lee, C. F., Caudal, A., Abell, L., Nagana Gowda, G. A. & Tian, R. Targeting NAD+ metabolism as interventions for mitochondrial disease. *Sci. Rep.* **9**, 3073 (2019).

40. Membrez, M. et al. Trigonelline is an NAD+ precursor that improves muscle function during ageing and is reduced in human sarcopenia. *Nat. Metab.* **6**, 433–447 (2024).

41. Guarente, L., Sinclair, D. A. & Kroemer, G. Human trials exploring anti-aging medicines. *Cell Metab.* **36**, 354–376 (2024).

42. Paşca, S. P. et al. A nomenclature consensus for nervous system organoids and assembloids. *Nature* **609**, 907–910 (2022).

43. Shi, X. & Janmey, P. A. Large polyacrylamide hydrogels for large-batch cell culture and mechanobiological studies. *Macromol. Biosci.* **23**, e2300042 (2023).

44. Mondrinos, M. J. et al. Surface-directed engineering of tissue anisotropy in microphysiological models of musculoskeletal tissue. *Sci. Adv.* **7**, eabe9446 (2021).

45. Osaki, T., Uzel, S. G. M. & Kamm, R. D. On-chip 3D neuromuscular model for drug screening and precision medicine in neuromuscular disease. *Nat. Protoc.* **15**, 421–449 (2020).

46. Uzel, S. G. et al. Microfluidic device for the formation of optically excitable, three-dimensional, compartmentalized motor units. *Sci. Adv.* **2**, e1501429 (2016).

47. Afshar Bakooshli, M. et al. A 3D culture model of innervated human skeletal muscle enables studies of the adult neuromuscular junction. *ELife* **8**, e44530 (2019).

48. Ko, E. et al. Matrix topography regulates synaptic transmission at the neuromuscular junction. *Adv. Sci.* **6**, 1801521 (2019).

49. Narayanan, N. et al. Harnessing nerve-muscle cell interactions for biomaterials-based skeletal muscle regeneration. *J. Biomed. Mater. Res. A* **109**, 289–299 (2021).

50. Correia, J. C. et al. Muscle-secreted neurturin couples myofiber oxidative metabolism and slow motor neuron identity. *Cell Metab.* **33**, 2215–2230.e8 (2021).

51. Benkert, P. et al. Serum neurofilament light chain for individual prognostication of disease activity in people with multiple sclerosis: a retrospective modelling and validation study. *Lancet Neurol.* **21**, 246–257 (2022).

52. Gaetani, L. et al. Neurofilament light chain as a biomarker in neurological disorders. *J. Neurol. Neurosurg. Psychiatry* **90**, 870–881 (2019).

53. Shi, Y. et al. Serum neurofilament light reflects cognitive dysfunctions in children with obstructive sleep apnea. *BMC Pediatr.* **22**, 449 (2022).

54. Foster, K. A., Margraf, R. R. & Turner, D. A. NADH hyperoxidation correlates with enhanced susceptibility of aged rats to hypoxia. *Neurobiol. Aging* **29**, 598–613 (2008).

55. Wang, X. et al. Deletion of Nampt in projection neurons of adult mice leads to motor dysfunction, neurodegeneration, and death. *Cell Rep.* **20**, 2184–2200 (2017).

56. Lundt, S. & Ding, S. Potential therapeutic interventions targeting NAD+ metabolism for ALS. *Cells* **13**, 1509 (2024).

57. Berven, H. et al. NR-SAFE: a randomized, double-blind safety trial of high dose nicotinamide riboside in Parkinson's disease. *Nat. Commun.* **14**, 7793 (2023).

58. Leng, Y. et al. Advances in in vitro models of neuromuscular junction: focusing on organ-on-a-chip, organoids, and biohybrid robotics. *Adv. Mater.* **35**, e2211059 (2023).

59. Sances, S. et al. Modeling ALS with motor neurons derived from human induced pluripotent stem cells. *Nat. Neurosci.* **19**, 542–553 (2016).

60. Van Meer, B. J. et al. Quantification of muscle contraction in vitro and in vivo using MUSCLEMOTION software: From stem cell-derived cardiomyocytes to zebrafish and human hearts. *Curr. Protoc. Hum. Genet.* **99**, e67 (2018).

Acknowledgements

Author contributions

Competing interests

The authors declare no competing interests.

Additional information

Supplementary information The online version contains supplementary material available at https://doi.org/10.1038/s41467-025-63736-0.

Correspondence and requests for materials should be addressed to Yun Lu, Jiao Li or Yuehua Liu.

Peer review information *Nature Communications* thanks Hadar Ben-Yoav, King-Hwa Ling and the other anonymous reviewer(s) for their contribution to the peer review of this work. A peer review file is available.

Reprints and permissions information is available at http://www.nature.com/reprints

Publisher's note Springer Nature remains neutral with regard to jurisdictional claims in published maps and institutional affiliations.